

Leveraging Teleconnections with Physics-Informed Graph Attention Networks for Long-Range Extreme Rainfall Forecasting in Thailand

Kiattikun Chobtham^a, Kanoksri Sarinnapakorn^a, Kritanai Torsri^a,
Prattana Deeprasertkul^a, Jirawan Kamma^a

^aHydro-Informatics Institute, Ministry of Higher Education, Science, Research and Innovation, Bangkok 10900, Thailand

Abstract

Accurate rainfall forecasting, particularly for extreme events, remains a significant challenge in climatology and the Earth system. This paper presents novel physics-informed Graph Neural Networks (GNNs) combined with extreme-value analysis techniques to improve gauge-station rainfall predictions across Thailand. The model leverages a graph-structured representation of gauge stations to capture complex spatiotemporal patterns, and it offers explainability through teleconnections. We preprocess relevant climate indices that potentially influence regional rainfall. The proposed Graph Attention Network with Long Short-Term Memory (Attention-LSTM) applies the attention mechanism using initial edge features derived from simple orographic-precipitation physics formulation. The embeddings are subsequently processed by LSTM layers. To address extremes, we perform Peak-Over-Threshold (POT) mapping using the novel Spatial Season-aware Generalized Pareto Distribution (GPD) method, which overcomes limitations of traditional machine-learning models. Experiments demonstrate that our method outperforms well-established baselines across most regions, including areas prone to extremes, and remains strongly competitive with the state-of-the-art. Compared with the operational forecasting system SEAS5, our real-world application improves extreme-event prediction and offers a practical enhancement to produce high-resolution maps that support decision-making in long-term water management.

Keywords: Graph Neural Networks, Orographic precipitation, Extreme Value Theory, Spatiotemporal modeling, Recurrent Neural Networks

1 Introduction

Climate change has led to more frequent and severe weather events, affecting the environment and society, and hence improving climate prediction remains challenging. Several studies in Numerical Weather Prediction (NWP) and Machine Learning (ML) have made significant advancements in climate modeling for short-term (one hour-15 days) or medium-term (2-6 weeks of sub-seasonal forecasting) climate predictions. In terms of long-term climate predictions, these produce forecasts

months in advance to address the challenges of water management in reservoirs and agricultural planning. This forecasting is feasible because some climate features within the Earth system evolve gradually. Their slower patterns are predictable over extended timescales. For example, teleconnections from Sea Surface Temperatures (SSTs) in the Niño 1+2, Niño 3 and Niño 4 regions (El Niño–Southern Oscillation climate index: ENSO) in the Pacific Ocean or the North Pacific area (Pacific Decadal Oscillation climate index: PDO) in specific years can significantly affect rainfall patterns in various areas during El Niño or La Niña events. The studies (Fuentes-Franco et al., 2016; Wang et al., 2014; Arcodia et al., 2020) provided insights into the statistical analysis of climate variables or climate indices, by examining historical trends and precipitation patterns at both global and regional scales in many regions.

In the northern peninsular Malaysia area, ENSO exerts a strong influence on the timing and intensity of the monsoon (Moten et al., 2014), affecting global rainfall distribution and the apparent length of the rainy season. Specifically in Thailand, the hydroclimate is governed by a monsoon regime. The principal rainy or wet season spans mid-May to mid-October during the Southwest monsoon, which advects humid air from the Indian Ocean and produces widespread heavy rainfall. In contrast, the Northeast monsoon transports colder and drier continental air from China into Thailand from October to December. The transition period from March to May is typically marked by rising temperatures as the region shifts from the Northeast to the Southwest monsoon, known as the monsoon onset period (Khedari et al. 2002; Chokngamwong & Chiu, 2006). However, the rainfall patterns in southern Thailand differ from those in other regions (Amnuaylojaroen, 2021). This is because the region is near the Intertropical Convergence Zone (ITCZ) and is impacted by the eastward-propagating wind patterns of the Madden-Julian Oscillation (MJO) and Boreal Summer Intraseasonal Oscillation (BSISO) (Chang et al. 2019). Therefore, a clear understanding of the Earth system is a critical step for developing accurate predictive models.

Classical dynamic weather forecasting models or physics-based NWP typically employ computer simulations for short-term or long-term forecasts (3-6 months) based on weather variables, e.g. SEAS5 (Johnson et al., 2019). SEAS5 is the fifth-generation seasonal forecasting system and a widely used public benchmark developed by the European Centre for Medium-Range Weather Forecasts (ECMWF). It couples the atmosphere of the Integrated Forecasting System (IFS) to ocean and sea-ice components with 91 vertical levels to produce probabilistic, long-range seasonal precipitation forecasts. The operational product uses a perturbation scheme to generate a 51-member ensemble and it issues monthly global seasonal outlooks at roughly 36-km horizontal resolution. However, these methods are often time-consuming and require substantial expert knowledge, potentially imposing strong mechanistic assumptions on the Earth system. Consequently, interest has shifted toward data-driven approaches based on ML methods.

ML models that leverage deep learning can uncover complex nonlinear spatiotemporal relationships. Recent studies have explored deep learning, for example, Graph Neural Networks (GNNs) (Scarselli et al., 2018), and physics-informed Neural Networks (PINNs) (Kurth et al., 2023), which can excel in prediction tasks. In terms of global short-term weather prediction, deep learning methods FourCastNet (Kurth, T et al., 2023; Bonev, B. et al., 2025), GraphCast (Lam et

al., 2023), Aardvark Weather (Allen et al., 2025), and Pangu Weather (Bi, K. et al., 2023) were introduced as compelling alternatives to NWP models. While the novel deep-learning model ClimeODE (Verma, 2024) was proposed to learn a spatiotemporal continuous-time process governed by atmospheric physics. Research recommendations emphasize that data-driven ML and traditional physical modeling can complement each other in predicting extreme events (Saha et al., 2024; Camps-Valls, 2023). However, the ML models remain limited to short-term predictions, and many models do not predict rainfall. Moreover, interpretability is an ongoing difficulty, as causal mechanisms are often difficult to extract from machine-learning black-box models. As a result, these models hinder practitioners from making decisions in real-world situations (Waqas et al., 2025). Methods from explainable AI and causal discovery algorithms (Kitson et al., 2023) can help elucidate the relative contributions of various climate drivers and their interactions in modulating climate (Runge et al., 2019; Du et al., 2024), but a causal model must be represented by a directed acyclic graph and time-series prediction remains particularly challenging (Ravuri et al., 2021).

In this work, we cast the long-term rainfall prediction problem in a specific region of Thailand into graph-structured models offering explainability that can be interpreted by humans. We enhance an attention mechanism to learn from spatiotemporal data with physics-informed GNNs called Attention-LSTM. The learning algorithm of the proposed model can automatically focus on important features and their spatial teleconnections. Moreover, we propose a novel Spatial Season-aware GPD method for extreme value analysis, paired with Attention-LSTM, to improve extreme rainfall prediction.

Our work consists of the following steps:

- 1) Construct and reanalyse graph-structured models based on physics-inspired initial edge features derived from orographic precipitation (details are given in Subsection 2.1), clusters of gauge stations and feature selection for each cluster.
- 2) Learn nonlinear relationships from spatiotemporal data with the proposed Attention-LSTM models for each cluster of gauge stations (details are given in Section 3).
- 3) Improve extreme rainfall prediction by mapping the predicted values with POT using the novel Spatial Season-aware GPD method (details are given in Subsection 4.1).

The paper is organised as follows: Section 2 describes related work, while Sections 3 and 4 present physics-informed Attention-LSTM and Spatial Season-aware GPD respectively, Section 5 describes dataset and experimental setup. Section 6 presents experimental results, and we provide our concluding remarks in Section 7.

2 Related Work

2.1 Orographic Precipitation

As mentioned in the introduction, various studies suggest integrating physics with data-driven ML. The simple thermodynamic equation of Smith's linear model (Smith, 2003), governed by the physics of orographic precipitation, provides the spectral formulation that captures the basic structure of rainfall fields. The formula is applicable to high-mountain meteorology as follows:

$$\hat{P}(k, l) = \frac{C_w i \sigma \hat{h}(k, l)}{(1 + i \sigma \tau_c)(1 + i \sigma \tau_h)} \quad (1)$$

where $\hat{P}(k, l)$ is the spectral transform of the precipitation field, C_w is the condensation-efficiency constant calculated using air density and saturation specific humidity, $\hat{h}(k, l)$ is the Fourier transform of the terrain elevation, τ_c is the conversion time scale from cloud water to rain (hydrometeors), τ_h is the time constant for hydrometeor fallout, k and l are wavenumbers, $\sigma = \text{U}k + \text{V}l$, U and V are zonal and meridional wind components, and i denotes the imaginary number. The orographic-precipitation formulation is the short-term precipitation governing equation for advection, conversion, and fallout. Precipitation is distributed downwind from each location over a distance equal to the product of the wind speed and the cloud time constant. Figure 1 shows a simple simulation of equation (1) where the wind speed is 40 m/s, τ_c is 1000, τ_h is 500, and the mountain height is 2000 m. For long-term climate forecasting, machine-learning models can potentially capture spatial teleconnections over these features to represent the underlying physical processes. Therefore, terrain elevation, the U and V variables should be included as model features.

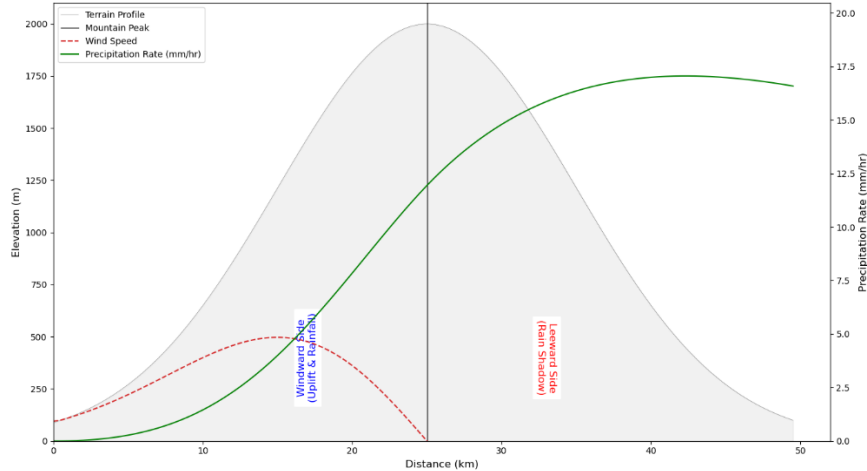


Figure 1. Simulation of the simple thermodynamic equation of Smith's linear model

2.2 Recurrent Neural Networks (RNNs) and Graph Neural Networks (GNNs)

Recent advancements in forecasting long-term climate variability have increasingly relied on ML and deep learning models. Recurrent Neural Networks (RNNs), LSTM, and Gated Recurrent Unit (GRU) were employed for sequence-to-sequence prediction (Hochreiter and Schmidhuber, 1997; Cho et al., 2014). Consequently, hybrid models (Waqas et al., 2024) using biorthogonal discrete wavelet transformation (Hammond et al, 2011) with LSTM (Wavelet-CNN-LSTM and Wavelet-LSTM) have shown superior performance in monthly gauge-rainfall predictions compared to traditional models. Recently, GNNs are a well-established neural network architecture designed for processing graph-structured data. GNNs can take input in the form of a directed or undirected graph describing the connectivity structure, making them more appropriate for spatial data that lack a regular grid in a non-Euclidean domain. This architecture learns node representations through a message-passing mechanism, followed by aggregation to produce an embedding for the entire graph. Shan et al. (2025) introduced a GNN incorporating physical edge features (edge

distance). This bridges physics-based understanding with interpretable AI. The GNN framework GraphCast embeds each node in a non-Euclidean domain (Lam et al., 2023), but the model is used for short-term weather forecasting with a 6-hour time-step prediction, and the number of autoregressive steps could be increased up to 3 days. However, this autoregressive prediction can lead to error propagation in long-term forecasting.

Several approaches using GNNs with spatiotemporal data were proposed to learn graph representations for supervised tasks, although the majority of applications have addressed traffic forecasting rather than weather forecasting. For example, Chen et al. (2022) modified Graph Convolutional Networks (GCNs) (Kipf & Welling, 2017) and LSTMs and proposed GC-LSTM to predict future links, achieving outstanding performance and outperforming state-of-the-art methods. GCNs were formulated for undirected graphs, operating on the normalised graph Laplacian. Their convolution is implemented using a localised first-order Chebyshev polynomial of the Laplacian (Kipf & Welling, 2017). Pareja et al. (2020) proposed EvolveGCN, which learns node embeddings over time by combining dynamic graphs with RNNs (two variants, EvolveGCN-H and EvolveGCN-O, use GRU and LSTM, respectively) to evolve the weights in GCNs, which serve as the hidden states of the RNN architecture. A Graph Multi-Attention Network (GMAN) was introduced to predict traffic conditions several steps ahead using a Transformer attention layer (Zheng et al., 2019). The model employed both spatial and temporal attention mechanisms to encode traffic features and generate output sequences. Wu et al. (2018) proposed Graph Attention LSTM (GAT-LSTM) to forecast traffic flow as a time-series problem on road networks. They constructed a directed graph of the road network and stacked multiple GAT-LSTM layers to learn from this structure, addressing the link-level traffic-forecasting problem.

Graph Attention Networks (GATs)

Since our approach applies GATs and LSTM to the rainfall-forecasting problem, we introduce preliminary information in the following subsections. Formally, we define static and dynamic graphs as follows:

A static graph $G = (V, E)$ consists of a set of nodes V and a set of edges E , while dynamic graphs can be represented as snapshot graphs at time t where $G_t = (V, E_t)$; $t \in [1, T]$. Attention and self-attention strategies are proven useful for tasks in Large Language Models (LLMs). GATs (Veličković et al., 2018) are an enhanced GCN architecture that utilizes an attention mechanism specifically designed to work with graph-structured data. GATs can assign different weights to nodes within the neighborhood without prior knowledge of edge weights.

Specifically, GATs capture weight matrices through an implicit attention mechanism. This allows more important nodes to receive higher weights during the neighborhood aggregation step. The approach is effective because it employs a self-attention mechanism on the nodes, determining the significance of the features of node i to those of node j . The attention coefficients (α_{ij}) are calculated using the following equations:

$$\mathbf{z}_i = \mathbf{W}_{node} * \mathbf{h}_i \quad (2)$$

$$\mathbf{g}_{ij} = \mathbf{W}_{edge} * \mathbf{f}_{ij} \quad (3)$$

$$\mathbf{e}_{ij} = \text{LeakyReLU}(\vec{a}^T (\mathbf{z}_i || \mathbf{z}_j || \mathbf{g}_{ij})) \quad (4)$$

$$\alpha_{ij} = \frac{\exp(e_{ij})}{\sum_{k \in \mathcal{N}_i} \exp(e_{ik})} \quad (5)$$

$$\mathbf{h}_i = \sigma \left(\frac{1}{K} \sum_{k=1}^K \sum_{j \in \mathcal{N}_i} \alpha_{ij}^k \mathbf{W}^k \mathbf{h}_j \right) \quad (6)$$

where \mathbf{W}_{node} and \mathbf{W}_{edge} are learnable weight matrices to transform node and edge features respectively, $\mathbf{h} = \{h_1, h_2, h_3, \dots, h_V\}$ and \mathbf{h}_i are node-features and node-feature embeddings respectively, \mathbf{z}_i is higher-level features of node i , \mathbf{g}_{ij} is higher level-features of the edge from node i to j , α_{ij} is the attention coefficient between node i and j , \mathbf{f}_{ij} is the edge feature for the edge from node i to j , V is the number of nodes, \vec{a} is a learnable weight vector, \mathcal{N}_i is a set of neighbors of node i , $||$ denotes the concatenation operation, σ denotes the sigmoid activation function and LeakyReLU denotes the Leaky Rectified Linear Unit activation function. GATs can be extended to employ multi-head attention using K independent attention mechanisms to enhance performance where the aggregated features from each head are concatenated or averaged.

3 Attention-LSTM

We propose a novel model, Attention-LSTM, that uses both spatial teleconnection and attention mechanisms, with edge features (\mathbf{f}_{ij}) reflecting the thermodynamic process of orographic precipitation at each time step. The attention coefficients assigned to each node feature dynamically impact rainfall stations over space and time. A key limitation is the absence of a ground truth graph structure or a dynamic data-generating process in the Earth system. Therefore, the assumption of our work is that our graph structure will remain static over time, while the calculated attention coefficients (α_{ij}) dynamically adjust the impact of each node feature and physics-informed edge features. To carry the message passing of the node embedding for the next time step, we employ GATs (described in Subsection 2.2) that can process graph structures. We modify LSTM, the classical RNN for capturing temporal relationships, where the hidden cell representing spatial teleconnection and spatial attention from GATs serves as the input to the LSTM.

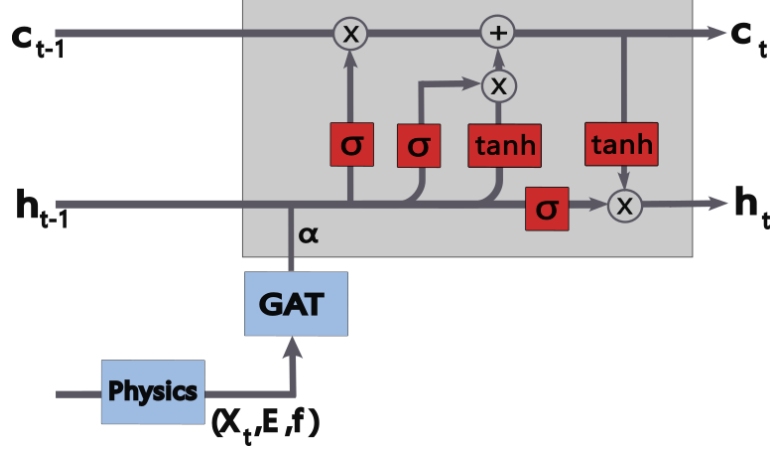


Figure 2. The Attention-LSTM architecture

3.1 Dynamic Attention Coefficients

Our novel approach introduces attention coefficients (weight matrices) of GATs into state-of-the-art LSTM. Static edges (E) of graph structures will be constructed using Pearson correlation as the statistical method, referred to as teleconnection. This served as feature selection for data-preprocessing in a ML process. The weight matrix ($W_{attention}$) represents dynamic attention coefficients given the graph structure. We use the LSTM in this work to update the hidden state over timestep t. The input information is the node embeddings (h_t) as hidden states of the LSTM. The framework is shown in Figure 2, and the formulas of Attention-LSTM are:

$$f_t = \sigma(GAT_\alpha(X_t) + h_{t-1} + b_f) \quad (7)$$

$$i_t = \sigma(GAT_\alpha(X_t) + h_{t-1} + b_i) \quad (8)$$

$$\tilde{c}_t = \tanh(GAT_\alpha(X_t) + h_{t-1} + b_c) \quad (9)$$

$$o_t = \sigma(GAT_\alpha(X_t) + h_{t-1} + b_o) \quad (10)$$

$$h_t = o_t * \tanh(c_t) \quad (11)$$

$$c_t = f_t * (c_{t-1}) + i_t * \tilde{c}_t \quad (12)$$

where $W_{attention} = \{\alpha_{ij}\}$ denotes the weight matrix calculated from the GAT model from equation (2) - (6), $E = \{a_{ij}\}$ denotes the adjacency matrix using specified teleconnections, \tanh is the hyperbolic tangent nonlinearity function, h_t denotes the node embedding at time step t, c_t denotes the long-term cell memory as learnable parameters at time step t, X_t is the input node feature at time step t, $b_{(f-o)}$ denotes the learnable bias matrices and GAT_α refers to GAT learning dynamic attention coefficients α_{ij} . We assume that the graph model remains static for each time step in this work. GATs explicitly incorporate edge features based on physics formulations. Therefore, we use the simulation of orographic precipitation from Subsection 2.1 as the physics-informed edge features for the edge from node i to node j using $f_{ij} = \hat{P}(k, l)$ from equation (1) to

represent the initial edge features of precipitation for each node j given the gauge-station elevation and climate variables at that location (U and V wind components).

3.2 GNN Model Reanalysis

Algorithm 1: Hierarchical clustering of rainfall stations

Input: monthly rainfall for each station, *latitude* and *longitude* for each station, distance d , components n in PCA

Output: clusters and their stations

- 1: *scaled_rain* \leftarrow Calculate the average monthly rainfall for each station as training data and normalize the data
- 2: *data_for_clustering* \leftarrow Reduce dimensionality using PCA with n components given *latitude*, *longitude* and *scaled rain*
- 3: *clusters* \leftarrow Calculate the Euclidean distance and determine clusters from *data_for_clustering* where the Euclidean distance between cluster centroid $<$ distance d

We reanalysed rainfall patterns in Thailand and found that rainfall stations should be clustered into different groups or clusters. We use the hierarchical clustering algorithm for rainfall stations in Algorithm 1 and construct static graph structures of Attention-LSTM for each cluster using a correlation test with a specific threshold. Algorithm 1 computes the average monthly rainfall for each station over the period, and the values are normalised. Principal Component Analysis (PCA) is then applied to reduce the data dimensionality using the normalised values and the station coordinates. Next, it computes Euclidean distances among the processed data. The final step of the algorithm performs hierarchical clustering proceeds by successively combining clusters whose centroid distances are less than the threshold d . Finally, we also incorporate lagged time using a statistical test of Granger Causality (details in Subsection 5.1), the test formulation is:

$$Y(t) = \sum_{i=1}^{lag} \alpha_i * Y(t-i) + \sum_{i=1}^{lag} \beta_i * X(t-i) + \epsilon_{y,t} \quad (13)$$

where α_i and β_i are coefficients, $X(t)$ denotes the climate index, and $Y(t)$ is rainfall at time t . If the tested p-value ≤ 0.1 , we reject the null that lagged X has no effect on Y and conclude that past X affects Y ; if $p > 0.1$, we fail to reject the null, indicating insufficient evidence that past X affects Y .

Algorithm 2 describes the training process for Attention-LSTM. The algorithm takes as input a static graph and training data with node features, edge, and edge features, along with the number of epochs, the window size, the horizon, and a list of hyperparameters. The list of hyperparameters includes multi-head attention K , number of layers, dropout probability, hidden size, and learning rate to be explored. Algorithm 2 begins by calculating the weight matrix from physics-informed edge features. Next, the GAT network with its configurations learns attention coefficients on the training dataset. The attention coefficients and graph embeddings are used as inputs to compute the predicted values. Finally, the algorithm calculates the loss function from the predicted and target values, and iteratively updates the learnable model weights. The model is trained by minimizing the Adaptive Huber loss (Huber, 1964). In standard Huber loss, the loss function behaves like mean squared error for small errors and like mean absolute error for large errors which aims to be robust to outliers in the data.

$$\text{Adaptive Huber Loss } L = (Y'_t, Y_t) = \begin{cases} \frac{1}{2} |Y'_t - Y_t|^2 & ; |Y'_t - Y_t| \leq \delta \\ \delta \left(|Y'_t - Y_t| - \frac{1}{2} \delta \right) & ; |Y'_t - Y_t| > \delta \end{cases} \quad (14)$$

where δ denotes to as the robustification parameter (Fan, Li and Wang, 2017)

Algorithm 2: Training algorithm of Attention-LSTM

Input: static graph with edge E, features X and target Y, station elevations, U and V wind components, window size W, horizon H, number of epochs N, learning rate r, dropout rate d, multi-head attention k, number of layers l, and hidden size z

Output: Trained model

```

1: List of snapshots t ← Split signals with window size W and target horizon H given X and Y
2:  $E_{\text{feature}} \leftarrow$  Simulate physics-informed initial edge features using equation (1) for each station j given U and V wind components, and station elevation
3: num_epoch = 0
4: While num_epoch < N do
5:   For each snapshot t do
6:     model ← Define Attention-LSTM model using equations (2) - (12) with  $X_t$ , E,  $E_{\text{feature}}$  and
      hyperparameters d, z, l and k
7:      $Y' \leftarrow$  model( $X_t$ , E,  $E_{\text{feature}}$ )
8:     Calculate Adaptive Huber Loss ( $Y'_t, Y_t$ ) using equation (14)
9:     Backpropagate and update learnable parameters with learning rate r.
10:    num_epoch ++
11: Return model

```

4 Extreme Value Analysis with Spatial Season-aware GPD

Extreme values refer to very large values or a very small values with low probability. In climate prediction, heavy rainfall or heat waves in a short period at a specific location can cause potential catastrophic effects. The limitations of deep learning are generally well understood that their prediction values ignore the extreme values or the outliers of the distribution due to few observations or small sample sizes (Sun et al., 2021; Ting, 2024; Camps-Valls et al., 2025). Therefore, we need approaches to specifically tackle extreme value estimation within the tail region of the relevant distribution. To improve extreme value accuracy, the state-of-the-art statistical technique Quantile Mapping (QM) is used as a simple bias correction method to align the distribution of model outputs with that of observational data (Maraun, 2016). This method specifically adjusts the probability density function (PDF) of model outputs to achieve better consistency with the PDF of observed data. However, its accuracy is limited when significant discrepancies exist between model-based and observational dataset. QM is particularly effective for bias correction in reanalysis dataset, especially for precipitation, though it remains unclear whether the mapping function is applicable for long-term forecasting.

In Extreme Value Theory (EVT), one fits a Generalized Pareto (GP) distribution to rainfall excesses above a properly selected threshold u . This approach is also referred to as Peaks-Over - Threshold. The theory suggests that if the Cumulative Distribution Function (CDF) of the scaled

excesses $[Y - u \mid Y > u]$ of random variable Y above threshold u converges to a nondegenerate distribution Q_u , then this CDF should have the GP form (Lucarini et al., 2016):

$$Q_u(y) = P[Y - u < y \mid Y > u] = \begin{cases} 1 - \left(1 + \xi \frac{(y-u)}{a_u}\right)^{-1/\xi} & ; \xi \neq 0 \\ 1 - e^{-\frac{(y-u)}{a_u}} & ; \xi = 0 \end{cases} \quad (14)$$

where u is the threshold used to determine the excesses of random variable Y (Y denotes rainfall in this study), ξ and a_u are the shape and scale parameters of the distribution.

4.1 Spatial Season-aware GPD

We propose a novel approach, Spatial Season-aware GPD, for identifying extreme rainfall values geographically across seasons. Spatial Season-aware GPD maps the ML-predicted rainfall values to the predicted extreme rainfall values given a function learned from observational training data. Because threshold selection is crucial and identifying a threshold for an extreme rainfall value for each station is very difficult, using a percentile automatically adapts the definition of extreme to the conditions (in this study, the percentile threshold is between 90-95). The GPDs from equation (14) are fitted for each station and its corresponding season, based on the spatial location of the stations. The season for each station in the cluster ($i \in Cluster$) in Thailand, as illustrated in Table 1, was determined by domain experts. To estimate of the shape and scale parameters, we use Maximum Likelihood Estimation (MLE) as the estimation is a commonly used method. During the wet season, predicted values that exceed the threshold with the application of the POT method are mapped using the fitted GP distributions. Note that with very small samples, MLE can be numerically unstable or biased. We fit the GPD only when the number of exceedances exceeds 10, and we impose a hard capability at the maximum observed value to prevent unphysical extrapolation.

Cluster	Season	Season - Month	Spatial Season-aware GPD for station i
1-4	Wet	SW monsoon (MJJAS), NE monsoon (OND)	$Q_{i,sw}(y), Q_{i,ne}(y)$
	Dry	Monsoon retreat (JFMA)	$Q_{i,dry}(y)$
5-12	Wet	Monsoon onset (MAM), Monsoon peak (JJASO)	$Q_{i,onset}(y), Q_{i,peak}(y)$
	Dry	Monsoon retreat (NDJF)	$Q_{i,dry}(y)$

Table 1. Seasonal classifications and application of Spatial Season-aware GPD by station i in Thailand ($i \in Cluster$)

Finally, the workflow of a real-world application of long-range rainfall forecasting based on physics, Attention-LSTM and Spatial Season-aware GPD mapping is shown in the end-to-end forecasting system in Figure 3. Data preprocessing retrieves rainfall from stations along with climate features, performs missing-data imputation, calculates climate indices, and simulates the physics-based estimates of orographic rainfall as edge features for Attention-LSTM. Hierarchical

clustering of rainfall stations and time-lag processing are performed to construct graph-structured models for each cluster. The graph structures and physics-informed edge features and processed tensor data are used to train Attention-LSTM on GPUs. Hyperparameters are fine-tuned to meet target accuracy, followed by Spatial Season-aware GPD extreme-value mapping of the predicted values. For inference, the deployed models are run on a High-Performance Computing (HPC) to generate interpolated maps with 12-month rainfall predictions.

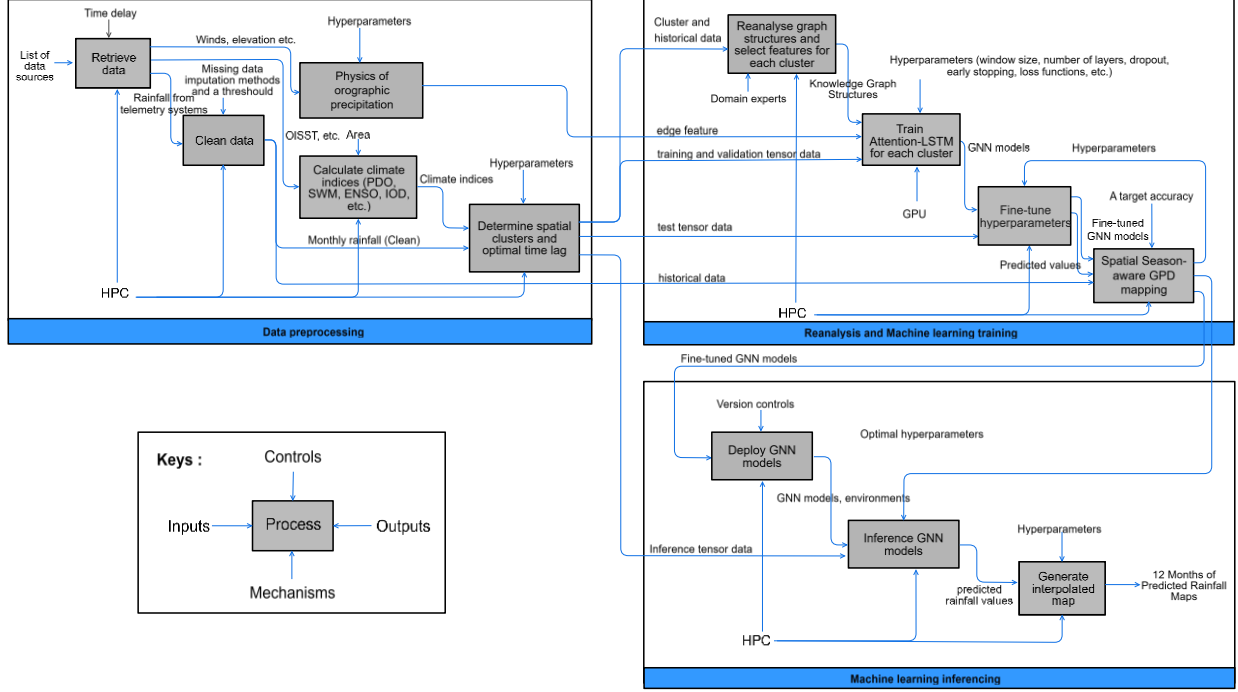


Figure 3. Workflow of the operational long-range rainfall forecasts based on physics-informed Attention-LSTM and Spatial Season-aware GPD extreme value mapping.

5 Dataset and Experimental Setup

5.1 Dataset and Graph Structure Modeling

We use seven climate indices detailed in Table 2, processed from NOAA OISST (Huang et al. 2021), together with historical rainfall data from the Hydro-Informatics Institute (HII) from 2014-2024 as inputs to the hierarchical clustering algorithm (Algorithm 1). Since MJO and BSISO are daily indices, we use the maximum amplitude to obtain the corresponding monthly values. The large number of HII stations covers most areas of Thailand, and hence the dataset is appropriate for clustering. Thai Meteorological Department (TMD) gauge stations from 1982-2024 are used as node features for Attention-LSTM. We also encode monthly periodicity of time t with trigonometric time embeddings as follows $\{\sin(\frac{2\pi t}{12}), \cos(\frac{2\pi t}{12})\}$. Note that forecasts of HII gauge stations are excluded from this experiment because of their limited sample size.

Climate feature	Description
Optimum Interpolation Sea Surface Temperature (OISST)	NOAA's long-term climate data record (Huang et al. 2021) blends observations from satellites, ships, buoys, and Argo floats onto a $0.25^\circ \times 0.25^\circ$ global grid. Missing values are interpolated to produce a spatially complete SST map.
U and V wind components	U is the eastward (zonal) wind component in meters per second; negative values indicate westward flow. V is the northward (meridional) wind component in meters per second; negative values indicate southward flow. Data are from the ERA5 reanalysis on a regular $0.25^\circ \times 0.25^\circ$ global grid.
Pacific Decadal Oscillation (PDO)	The SST Anomaly (SSTA) pattern represents Pacific climate variability. The PDO index is defined as projections of monthly mean SST anomalies onto their first Empirical Orthogonal Function (EOF) vectors in the North Pacific. The North Pacific area is approximately covered by: 20°N - 65°N , 120°E - 100°W .
Indian Ocean Dipole Mode Index (DMI)	The SSTA difference between the western (50°E - 70°E , 10°S - 10°N) and southeastern (90°E - 110°E , 10°S to equator) regions of the tropical Indian Ocean is weighted by latitude.
Oceanic Niño Index (ONI)	The SSTA averaged in the east-central equatorial Pacific Ocean (Niño 3.4: 5°S - 5°N , 170°W - 120°W).
South West monsoon Index (SWM)	The newly calculated SST difference between area A (87°E - 91°E , 20°N - 21°N) and area B (90°E - 95°E , 8°S - 10°S) in the tropical Indian Ocean.
North East monsoon Index (NE)	The newly calculated SST difference between area A (10 - 16.25°N , 110 - 118.75°E ; 8.75 - 10°N , 108.75 - 116.25°E ; 7.5 - 8.75°N , 107.5 - 115°E) and area B (3.75 - 6.25°N , 103.75 - 106.25°E) regions (Moten et al., 2014) in the South China Sea and Gulf of Thailand
Real-time Multivariate MJO series (RMM1)	The major fluctuation in tropical weather occurs on weekly to monthly timescales. The MJO can be characterized as an eastward-moving pulse of cloud and rainfall near the equator that typically recurs every 30 to 60 days. It is calculated using multivariate EOF (MV-EOF) of Outgoing Longwave Radiation (OLR) and zonal wind at 850 hPa (U850), which identifies two modes of interannual variability of the MJO.
Boreal Summer Intraseasonal Oscillation (BSISO)	BSISO strongly modulates sub-seasonal to seasonal rainfall variability. It refers to MV-EOF analysis of daily anomalies of OLR and zonal wind at 850 hPa (U850) in the region 10°S - 40°N , 40° - 160°E , for the extended boreal summer (May-October) season over the 30-year period 1981-2010.
Multivariate ENSO Index (MEI)	EOF analysis is performed on five different variables (Sea Level Pressure, SST, zonal and meridional components of the surface wind, and OLR) over the tropical Pacific basin (30°S - 30°N and 100°E - 70°W).

Table 2. Climate features used in the study

Following the spectral method of orographic precipitation (Subsection 2.1), we simulate orographic rainfall using each TMD gauge station elevation and ERA5 monthly average U and V wind components at 200 hPa, following the study of Saha et al. (2024) for 1982–2024. These serve as the Attention-LSTM's physics-informed initial edge features. For this preliminary simulation, we assume that conversion and fallout are fast, and hence $\tau_c = \tau_h = 0$. Since terrain gradients are out of scope in this study and simulating for all scenarios where a station lies on the windward or leeward side relative to the wind direction is generally computationally expensive. We simply approximate the slope magnitude using each station elevation. To construct the GNN edges, we manually define a static graph structure, and some examples are shown in Figure 5. Each climate

feature influences rainfall at individual stations through spatial teleconnections and temporal relationships. The selection of climate indices is based on feature-selection criteria using Pearson correlation. We construct a teleconnection when the average absolute correlation is higher than 0.4. We incorporate domain knowledge into the GNN edges because some climate indices evolve gradually. For example, the phase of the PDO typically evolves slowly. Therefore, feature selection based solely on Pearson correlation is not reliable for PDO; instead, hard constraints from domain experts are applied to ensure that PDO's influence on ENSO indices (e.g., ONI and MEI) is properly reflected (Fuentes-Franco et al., 2016).

To perform long-term rainfall forecasting (1–12 months ahead), missing rainfall values for each station are imputed using the monthly median. We exclude TMD stations that report less than 80% of their data for each month across the study period; as a result, 74 TMD stations are retained for the experiments. The full dataset (1982–2024) in Table 3 is split into two folds as the monthly rainfall sample size is very limited and the training cost for all hyperparameter combinations (grid search) is computationally expensive. Final performance is reported by averaging evaluation metrics across both test sets, stations, and horizons, reducing the risk of overfitting to specific La Niña (2021) or El Niño (2024) events within particular time windows. All HII stations in Thailand are clustered into 12 regions and mapped to the locations of the TMD stations; each TMD cluster is then used to train a single model per cluster, rather than training separate models for each station. Therefore, parallel training of all models offers a substantial reduction in computational time.

Moreover, we incorporate lagged effects for each climate feature using the Granger Casualty test (Granger, 1969) of equation (13) evaluated with the χ^2 test. We consider a teleconnection present when the test p-value is below a significance threshold of 0.1, indicating that the lagged influence of the teleconnection improves each station-level rainfall predictability for each cluster in Thailand.

Stations	The clusters and High-Quality (HQ) stations	Training, validation data and test data
TMD Station (132)	All HQ station: (74)	Fold 1: 1 (6) Training data (1982-2019): 456 months 2 (5) Validation data (2020): 24 months 3 (3) Test data: (2021): 24 months 4 (1) 5 (3) 6 (7) 7 (9) 8 (15) 9 (17) 10 (1) 11 (0) 12 (7)
		Fold 2: Training data (1982-2022): 492 months Validation data (2023): 24 months Test data: (2024): 24 months

Table 3. Training, validation data, and test data used in the study

5.2 Experimental Setup

In the experiment, we use a 24-month input window and a 12-month prediction horizon throughout the paper. Training hyperparameters are as follows: hidden layer sizes = [16, 32, 64]; the number of epochs = 200 with early stopping (patience=50) on the validation set; the number of GAT multi-heads = [1, 4, 8, 16]; the number of LSTM layers = [1, 2, 3]; and the dropout rate = [0, 0.2, 0.5].

Chebyshev filter sizes for GC-LSTM and EvolveGCN = [2, 3, 4, 5]. We use the bior1.3 wavelet at level 2 as the decomposition function for Wavelet-LSTM. All models are trained with the Adaptive Huber loss in equation (14) with a learning rate of 0.01 and $\delta = 1$.

We evaluate six models: Attention-LSTM without physics or Spatial Season-aware GPD mapping denoted as Attention-LSTM (without physics and GPD), Attention-LSTM, LSTM, Wavelet-LSTM, GC-LSTM, and EvolveGCN (EvolveGCN-O) implemented in PyTorch and PyTorch Geometric Temporal, with Python 3.8. All experiments are conducted on a HPC system equipped with a 32-core Intel Xeon CPU at 2.3 GHz, 64 GB of RAM, and six NVIDIA V100 GPUs.

5.3 Evaluation Metrics

We use three evaluation metrics: Root Mean Squared Error (RMSE), Nash–Sutcliffe Efficiency (NSE), and accuracy to assess the prediction performance of each approach. RMSE is calculated as:

$$RMSE = \sqrt[2]{MSE}, MSE = \frac{\sum (y_{i,t} - \hat{y}_{i,t})^2}{n}$$

The accuracy and Mean Absolute Percentage Error (MAPE) are calculated as follows:

$$Accuracy = 100 - MAPE = 100 - \frac{\sum (|y_{i,t} - \hat{y}_{i,t}| / y_{i,t})}{n} \times 100$$

Because MAPE is undefined when $y_{i,t}=0$, we use the Symmetric Mean Absolute Percentage Error (SMAPE), defined as:

$$SMAPE = \frac{\sum (2 \frac{|y_{i,t} - \hat{y}_{i,t}|}{|y_{i,t}| + |\hat{y}_{i,t}|})}{n} \times 100$$

The NSE is calculated as:

$$NSE = 1 - \frac{\sum (y_{i,t} - \hat{y}_{i,t})^2}{\sum (y_{i,t} - \bar{y}_{i,t})^2}$$

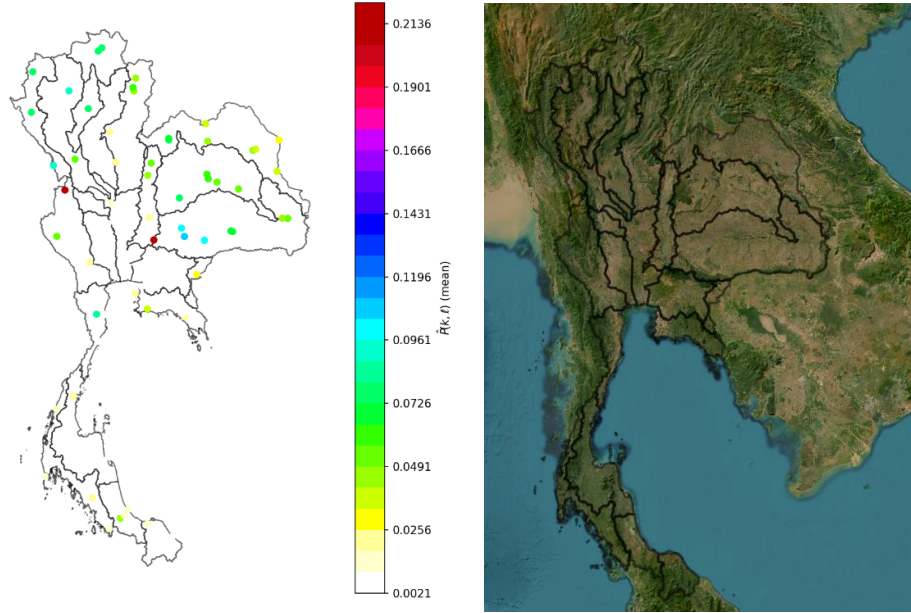
where $y_{i,t}$ is the observed rainfall at station i and time t , $\hat{y}_{i,t}$ is the predicted rainfall, $\bar{y}_{i,t}$ is the mean observed rainfall at station i over time, and n is the total number of stations and time steps. $NSE < 0$ indicates that the predictive skill is worse than using the mean observed rainfall.

6. Empirical Results

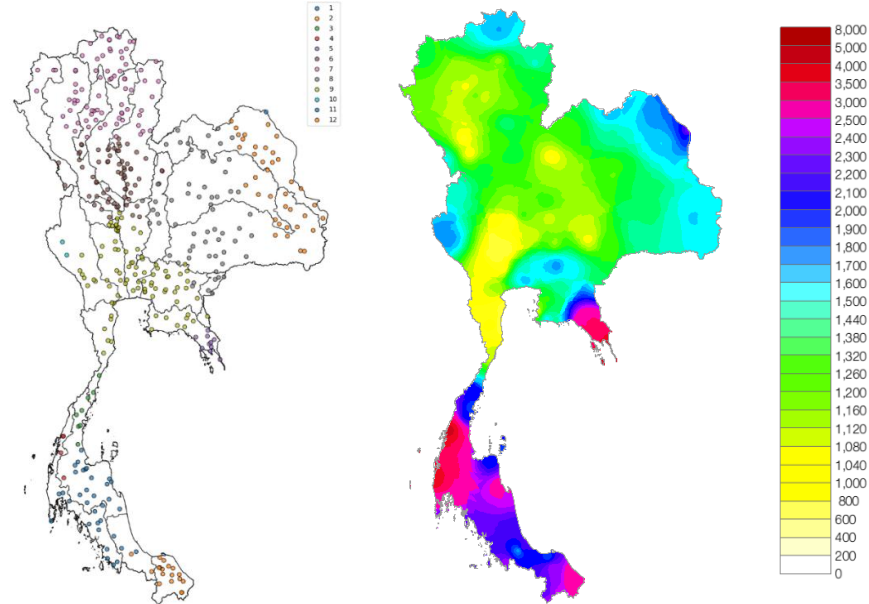
Based on dataset and the experimental setup in Section 5, we report the graph-based model results in Subsection 6.1. We then present statistics of Spatial Season-aware GPD mapping in Subsection

6.2 and compare predictive skill with related work in Subsection 6.3. Finally, Subsection 6.4 presents operational forecasts evaluated against the ECMWF SEAS5 seasonal forecasts.

6.1 GNN Model Interpretability for Each Cluster of Stations



(a) The spectral transform of the precipitation $\hat{P}(k, l)$ for each TMD rainfall station, simulated using ERA5 data spanning 1982–2024, compared with orography and the land-sea boundary in Thailand.



(b) Twelve-cluster results for HII rainfall stations and river basins, obtained by hierarchical clustering of HII rainfall stations (Algorithm 1), compared with the 30-year average TMD rainfall in Thailand (1991-2020).

Figure 4. Reanalysis graph-based structure (a) the spectral transform of the precipitation $\hat{P}(k, l)$ and (b) twelve-cluster areas for HII rainfall stations

The spectral transform of precipitation $\hat{P}(k, l)$ for each TMD rainfall station, simulated using ERA5 U and V wind components for 1982–2024, is shown in Figure 4a. A clear relationship between precipitation and high elevation is apparent, for example, the red-highlighted stations near Pak Chong District, Nakhon Ratchasima and Umphang District, Tak. Monthly rainfall at each HII station serves as input to the hierarchical clustering algorithm. The results show that the 12-cluster areas indicate the spatial pattern of average monthly rainfall and geography across Thailand (Figures 4a and 4b). For example, in Figure 4b, Clusters 1 and 3 refer to station areas in Southern Thailand facing the Gulf of Thailand, while Cluster 4 represents areas along the Indian Ocean. Cluster 2 lies in the area closest to the ITCZ. Cluster 11 contains only one station in Nong Khai province, which is frequently lies along storm paths. However, when we applied this clustering area to TMD stations, the sample size was too small to be used in the experiment.

For each cluster, we construct station-level graph structures using Pearson correlation and time-lag tests from monthly data. We define a teleconnection when the average absolute correlation during extreme events is higher than 0.4 and the time-lagged correlation is statistically significant (p -value < 0.1 ; see details in Appendix A1-A2). The differences in teleconnections between the models of Clusters 1 and 8 are BSISO and PDO. This aligns with the studies by Abatan et al. (2023) and Kikuchi (2021), which found that BSISO modulates sub-seasonal to seasonal rainfall in Northeast Thailand and is characterized by an elongated convective band orienting from the northwest to the southeast. All graph structures are reported in Appendix B.

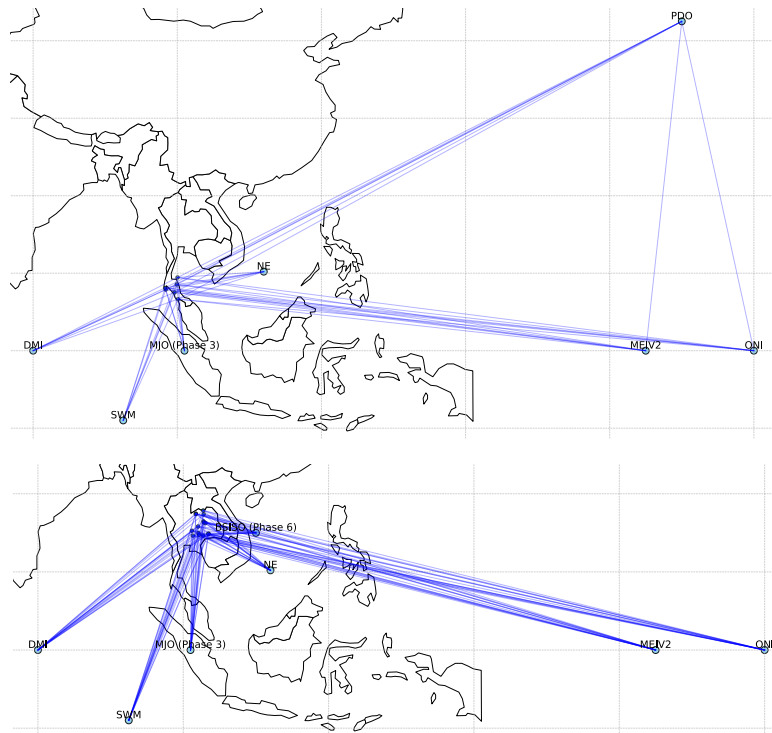


Figure 5. Examples of reanalysis graph-based structures of GNN models showing their stations as nodes and their teleconnections as edges in Cluster 1 (a) where DMI and PDO are lagged 1 by month and MEIV2 is lagged by 2 months and Cluster 8 (b) where MEIV2 is lagged by 3 months

6.2 Results of Spatial Season-aware GPD for TMD stations

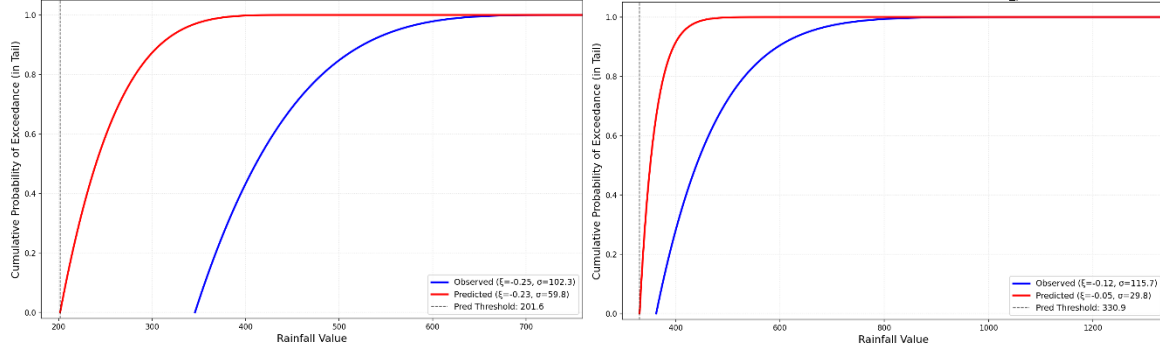
We perform Spatial Season-aware GPD mapping (Subsection 4.1) to analyse extreme values. Table 4 reports the GPD parameters, estimated from MLE for examples of stations and seasons in Clusters 1 and 8, using the threshold at the 95th percentile ($Q = 95$). Exceedances refer to the number of observations above Q (i.e., extreme rainfall events). Because the same percentile Q is applied to each station’s training time series, the number of exceedances for each season is the same across stations.

For station 567201 in Cluster 1, the observed threshold u in the NE monsoon is 345.8 mm/month and in the SW monsoon is 362.7 mm/month. The predicted threshold u computed from the fine-tuned Attention-LSTM (see details in Table 6), given training data (Fold = 2), is 201.6 mm ($Q_{i,NE}(y)$) in the NE monsoon and 330.9 mm/month ($Q_{i,SW}(y)$) in the SW monsoon. For station 387401 in Cluster 8, the observed u is 283.8 mm ($Q_{i,peak}(y)$) during the monsoon peak, and the predicted u is 244.73 mm/month ($Q_{i,peak}(y)$) during the monsoon peak. These results indicate that the ML-predicted values are typically lower than the observed extreme rainfall. The charts of Cumulative Distribution Functions (CDFs) of GPD are shown in Figure 6. These patterns indicate a consistent underestimation of the tail by Attention-LSTM, most pronounced during the NE-monsoon months of Cluster 1 and during the monsoon-peak months of Cluster 8.

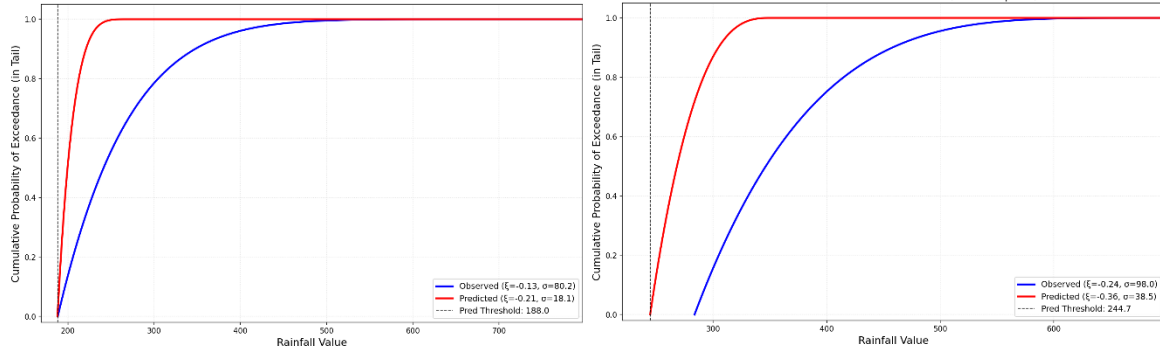
Consequently, Spatial Season-aware GPD mapping is particularly valuable for adjusting predicted extremes upward during the monsoon and monsoon-onset seasons. This offers a smooth mapping function for long-term rainfall forecasting. However, ($Q_{i,dry}(y)$) should not be applied during the dry season in these clusters.

Node	Season	Observation				Prediction of Attention-LSTM			
		u	ξ	a_u	exceedances	u	ξ	a_u	exceedances
Cluster 1									
567201	Dry	164.9	0.08	64.14	26	221.1	-0.29	25.29	23
	NE monsoon	345.8	-0.25	102.35	20	201.6	-0.23	59.84	18
	SW monsoon	362.7	-0.12	115.68	33	330.9	-0.05	29.83	29
Cluster 8									
387401	Dry	23.1	0.24	14.21	26	39.77	-0.21	24.5	23
	Monsoon onset	188.3	-0.13	80.22	20	188.02	-0.21	18.1	17
	Monsoon peak	283.8	-0.24	98.03	33	244.73	-0.36	38.5	29

Table 4. The GPD fitted parameters obtained using MLE for the stations and their season in Clusters 1 and 8 where percentile Q is 95.



(a) CDFs for station 56720 in the NE monsoon season (b) CDFs for station 56720 in the SW monsoon



(c) CDFs for station 387401 in the monsoon onset (d) CDFs for station 387401 in the monsoon peak season

Figure 6. Example plots of CDFs of GPD for sample stations and their wet seasons where percentile is 95

6.3 Predictive Performance Metrics for TMD Stations

Table 5 details the best performance achieved by each algorithm and the eleven meteorological clusters of TMD stations when tuning the hyperparameters for specific metrics (accuracy, RMSE or NSE). The optimal dropout, number of layers, hidden layer size, and multi-head settings when using optimizing accuracy are shown in Table 6. The results illustrate averages over stations within each cluster and forecast horizons. We evaluated Attention-LSTM (without physics and GPD) and the physics-informed Attention-LSTM with Spatial Season-aware GPD mapping at two exceedance cutoffs percentiles ($Q = 90, 95$), and assess the performance against baseline LSTM, Wavelet-LSTM, GC-LSTM, and EvolveGCN models. Note that Spatial Season-aware GPD mapping does not improve the performance of the competing approaches, and hence the results are not shown in the table. Overall, Attention-LSTM achieves the highest average accuracy across all clusters. Attention-LSTM mostly outperforms the competing algorithms in terms of Accuracy, RMSE, and NSE. This indicates that Attention-LSTM with physics and the Spatial Season-aware GPD mapping tends to yield higher performance metrics in most clusters among the competing approaches: LSTM, Wavelet-LSTM, GC-LSTM, and EvolveGCN.

Specifically, for averaged accuracy over Clusters 1–4, where the regimes experience more extreme rainfall, the maximum average accuracy (tuned models) of Attention-LSTM ($Q = 95$) is 71.46% compared with 57.90% for LSTM, 43.34% for Wavelet-LSTM, 57.12% for GC-LSTM, and 52.14% for EvolveGCN. The empirical results show that the attention mechanism, the physics

of orographic precipitation, and Spatial Season-aware GPD mapping effectively improve predictive skill compared to other models. This is because the GNN can dynamically update the spatial weights informed by physics and temporal attention weights for teleconnections between ENSO (ONI, MEIV2), DMI, monsoon indices (SWM, NE), and sub-seasonal to seasonal variability (BSISO, MJO). However, the averaged accuracy results over Clusters 5–12 show that Attention-LSTM ($Q = 90$) and LSTM perform comparably (70.1% and 68.11% respectively), reflecting heterogeneity in teleconnection strength across different regions, as the regimes of Clusters 5–12 experience fewer extreme rainfall events than those of Clusters 1–4.

Averaged across clusters, Attention-LSTM ($Q = 95$) achieves the highest mean accuracy (71%) compared with LSTM (64%), indicating consistent benefits from incorporating the physics of orographic precipitation and post-processing of predicted extremes with the Spatial Season-aware GPD tail mapping. Mapping the tail at $Q = 95$ improves accuracy by 7.1% over Attention-LSTM (without physics and GPD) and by 6.9% over $Q = 90$. Relative to competing models in the southern Clusters 1–4, Attention-LSTM ($Q = 95$) outperforms LSTM by 23.4%, Wavelet-LSTM by 64.9%, GC-LSTM by 25.1%, and EvolveGCN by 37.1%. These gains indicate that tail-focused processing enhances predictive skill, consistent with the importance of rainfall extremes. Moreover, the stronger threshold ($Q = 95$) yields the most pronounced advantage in this region.

GPD mapping and physics markedly lower the average RMSE in several clusters: for example, with Attention-LSTM ($Q = 90$), RMSE decreases from 127.99, 99.15, 155.77, and 147.97 mm/month to 103.32, 62.53, 70.17, and 115.00 mm/month in Clusters 1–4 respectively. Compared with the LSTM baseline, RMSE with Attention-LSTM ($Q = 90$) is 62.53 versus 98.52 for LSTM in Cluster 2; 70.17 versus 115.03 in Cluster 3; 115.00 versus 145.22 in Cluster 4; 52.97 versus 54.79 in Cluster 7; 60.02 versus 66.57 in Cluster 8, and 55.11 versus 86.76 in Cluster 10. In contrast, LSTM shows slightly better RMSE values of 94.54, 132.18, and 54.15 mm/month in Clusters 1, 5, and 6, respectively. These results indicate that while tail mapping often enhances magnitude fidelity, its effectiveness depends on local rainfall distributions. Attention-LSTM ($Q = 90$) achieves the highest average NSE in most clusters (e.g., Cluster 2: 0.93; Cluster 4: 0.90; Cluster 5: 0.86; Cluster 7: 0.81; Cluster 8: 0.70; Cluster 10: 0.89), indicating improved correspondence between predicted and observed rainfall compared with using simple averages of observed rainfall values. However, some clusters show a slight edge for LSTM (e.g., Cluster 1: 0.79; Cluster 6: 0.69).

In terms of computational time, models use different hyperparameter sets with early stopping enabled, and hence the training time for each hyperparameter combination and total run time is not directly comparable. The average time per epoch for Attention-LSTM, Wavelet-LSTM, GC-LSTM, LSTM, and EvolveGCN is 1.24 sec, 1.53 sec, 2.39 sec, 1.06 sec and 1.17 sec, respectively.

Cluster (stations)	Maximum average accuracy						
	Attention-LSTM (without physics and GPD)	Attention- LSTM (Q = 90)	Attention- LSTM (Q = 95)	LSTM	Wavelet- LSTM	GC-LSTM	Evolve- GCN
1 (TMD: 6)	63.36	65.94	67.46	64.90	39.48	59.34	52.52
2 (TMD: 5)	60.76	71.78	71.68	48.71	42.62	61.50	53.82
3 (TMD: 3)	62.70	66.24	66.58	52.82	42.54	53.56	49.33
4 (TMD: 1)	73.99	80.20	80.12	65.15	48.72	54.09	52.87
5 (TMD: 3)	72.29	71.85	71.95	69.44	42.27	42.58	60.47
6 (TMD: 7)	64.43	65.86	66.13	67.73	55.40	34.82	58.71
7 (TMD: 9)	69.77	73.39	73.40	72.08	55.94	41.23	66.80
8 (TMD: 15)	66.41	67.20	67.06	65.48	61.98	34.52	63.32
9 (TMD: 17)	65.57	65.30	65.17	64.21	64.45	37.48	60.69
10 (TMD: 1)	55.31	75.24	74.94	68.58	38.43	39.67	65.65
11 (TMD: 0)	-	-	-	-	-	-	-
12 (TMD: 7)	70.26	71.86	71.86	69.28	66.73	42.11	66.63
Minimum average RMSE (mm/month)							
1 (TMD: 6)	127.99	103.32	99.06	94.54	179.11	126.90	160.90
2 (TMD: 5)	99.15	62.53	64.43	98.52	140.70	86.96	128.56
3 (TMD: 3)	155.77	70.17	70.93	115.03	173.32	151.41	157.62
4 (TMD: 1)	147.97	115.00	116.87	145.22	142.15	133.96	186.85
5 (TMD: 3)	192.49	139.27	138.15	132.18	240.46	200.37	206.01
6 (TMD: 7)	59.63	58.87	57.97	54.15	62.32	59.59	68.28
7 (TMD: 9)	56.13	52.97	53.02	54.79	65.30	55.37	62.93
8 (TMD: 15)	70.61	60.02	60.23	66.57	72.32	69.79	75.50
9 (TMD: 17)	63.03	56.65	56.37	57.32	60.97	59.67	67.85
10 (TMD: 1)	124.42	55.11	57.01	86.76	158.74	100.23	118.27
11 (TMD: 0)	-	-	-	-	-	-	-
12 (TMD: 7)	68.71	58.32	57.72	67.73	71.86	59.91	76.61
Maximum average NSE							
1 (TMD: 6)	0.60	0.74	0.74	0.79	-0.01	0.56	0.34
2 (TMD: 5)	0.53	0.93	0.92	0.46	0.04	0.63	0.48
3 (TMD: 3)	0.27	0.67	0.68	0.60	-0.01	0.29	0.23
4 (TMD: 1)	0.71	0.90	0.90	0.66	0.00	0.68	0.39
5 (TMD: 3)	0.63	0.86	0.86	0.83	-0.03	0.66	0.57
6 (TMD: 7)	0.65	0.65	0.68	0.69	0.61	0.65	0.55
7 (TMD: 9)	0.56	0.81	0.80	0.71	0.47	0.72	0.58
8 (TMD: 15)	0.62	0.70	0.70	0.64	0.58	0.61	0.55
9 (TMD: 17)	0.61	0.67	0.68	0.67	0.63	0.64	0.54
10 (TMD: 1)	0.42	0.89	0.88	0.72	0.06	0.65	0.48
11 (TMD: 0)	-	-	-	-	-	-	-
12 (TMD: 7)	0.70	0.77	0.78	0.74	0.67	0.75	0.65

Table 5. The maximum average accuracy, the minimum average RMSE, and the maximum average NSE accuracy across all horizons and TMD stations for each of the seven tuned models for each hyperparameter setting. The best performance metrics are shown in bold.

Therefore, the explicit tail-mapping method; Spatial Season-aware GPD is effectively combined with the attention mechanism of Attention-LSTM and physics. It generally yields the highest accuracy and NSE. However, the reductions in error magnitude occur primarily in southern Thailand (Clusters 1–4), where heavy-rainfall regimes make tail mapping especially beneficial. However, not all clusters benefit equally. These findings support the effectiveness of physics-

informed Attention-LSTM paired with Spatial Season-aware GPD mapping for long-range monthly rainfall prediction in Thailand. In a few cases, retaining a simple LSTM remains superior for RMSE and NSE, highlighting discrepancies between these metrics and accuracy. Moreover, both GC-LSTM and EvolveGCN use graph convolutional models whose Chebyshev polynomial spectral filters may not be appropriate for long-range rainfall prediction.

Cluster	Multi head	Hidden Size	Number of layers	Dropout
1	8	64	1	0.2
2	1	64	1	0.5
3	8	64	1	0
4	8	32	3	0.5
5	16	16	1	0
6	1	64	1	0
7	4	16	2	0.2
8	16	16	1	0.2
9	8	16	2	0
10	4	32	1	0
12	4	16	3	0.2

Table 6. Optimal hyperparameters of the fine-tuned Attention-LSTM ($Q = 95$) model using accuracy for each cluster of TMD stations.

6.4 Real-world Applications compared with ECMWF Seasonal Forecasts

In ECMWF’s operational seasonal forecasting system from SEAS5, probabilities of precipitation anomalies or the mean of precipitation over 51 ensembles summarise the expected climate over the coming months from a statistical view of potential weather. The operational web-based products are available here.

(https://charts.ecmwf.int/products/seasonal_system5_standard_rain?area=AUSG&stats=ensm)

To illustrate real-world applications in this study, we show out-of-sample data from 74 ground-truth TMD stations for March–August 2025 in this subsection. As shown in Figure 3, inputs of the end-to-end workflow for long-range rainfall forecasts include gauge rainfall, reanalysis data (e.g., OISST, U and V components of wind). The system processes climate indices (PDO, SWM, ONI, DMI, etc.) and computes initial edge features using Smith’s linear model. It generates monthly rainfall forecasts up to 12 months ahead. Model development and inference are conducted in version-controlled environments on HPC/GPU infrastructure, with fine-tuned hyperparameters to maximise accuracy.

We generate high-resolution forecasting maps by interpolating TMD gauge observations using the Inverse Distance Weighting (IDW) method. Forecasts in Figures 7-12 are generated from ECMWF SEAS5 and from our operational long-range rainfall forecasting system (<https://ai-long-range.hii.or.th/rain/forecast.html>), which employ the Attention-LSTM model ($Q = 95$). This is because Attention-LSTM model ($Q = 95$) provides the highest average accuracy across clusters (Table 5). Both predictions are initialized in March 2025 with a six-month lead time, covering

March through August 2025. Because the inputs and outputs of ECMWF SEAS5 and our proposed model are different, a direct comparison is not strictly fair. For a preliminary assessment, we evaluated the 74 gauge stations as sample grid points. For monthly RMSE at these stations for March–August 2025, Attention-LSTM ($Q = 95$) achieves a better RMSE than SEAS5 by 24.19 mm/month on average and yields a better RMSE in about 66% of cases. SEAS5 slightly outperforms Attention-LSTM in April and May. These months are known as the transition period from monsoon onset to peak. Considering average rainfall across stations, Attention-LSTM ($Q = 95$) is within around $\pm 10\%$ of ground truth in four months (April, June, July, August) whereas SEAS5 is within $\pm 10\%$ only in May. Overall, these results indicate that Attention-LSTM ($Q = 95$) is suitable for operational downscaling for water-management applications, while the native SEAS5 resolution is comparatively coarse for community-level water management decision-making in real-world applications.

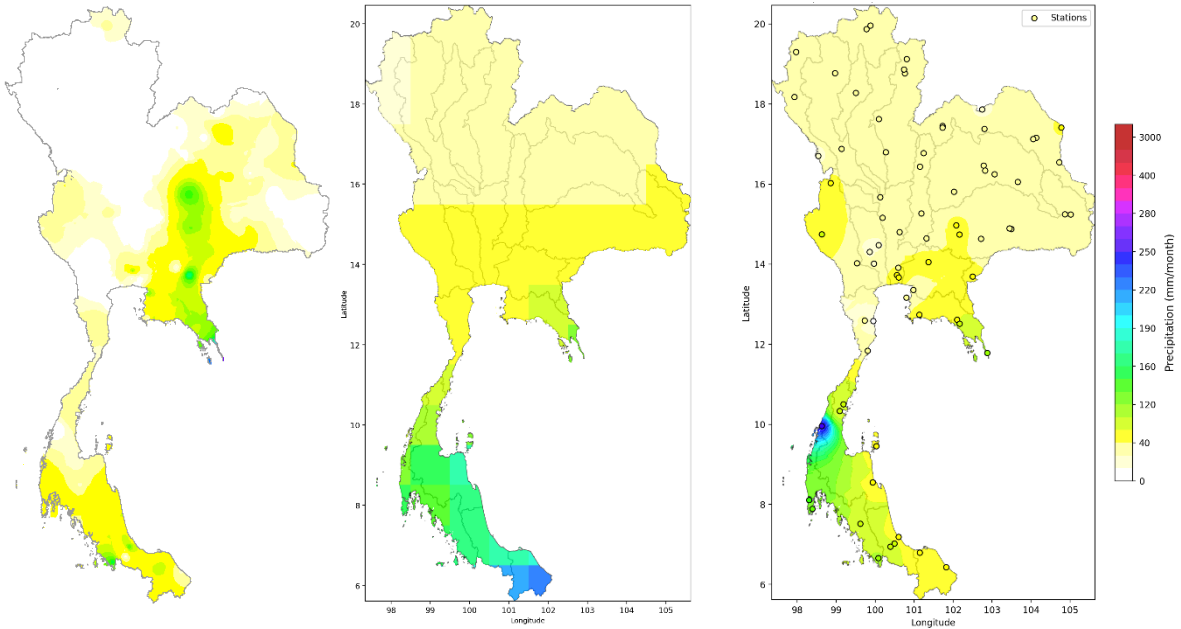


Figure 7. Monthly total precipitation for March 2025. Left: ground truth (average rainfall = 39.13 mm/month) Middle (prediction): SEAS5 (RMSE = 58.97 mm/month, average rainfall = 65.89 mm/month). Right (prediction): Attention-LSTM ($Q = 95$) (RMSE = 50.11 mm/month, average rainfall = 46.92 mm/month).

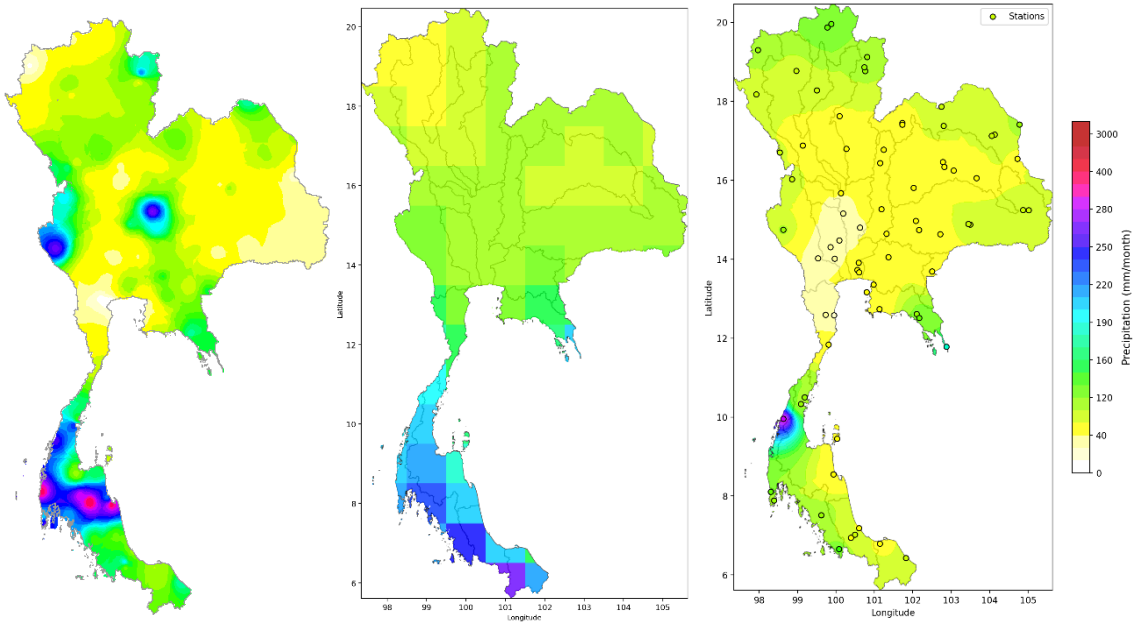


Figure 8. Monthly total precipitation for April 2025. Left: ground truth. (average rainfall = 104.32 mm/month) Middle (prediction): SEAS5 (RMSE = 58.78 mm/month, average rainfall = 128.49 mm/month). Right (prediction): Attention-LSTM (Q = 95) (RMSE = 59.80 mm/month, average rainfall = 113.53 mm/month).

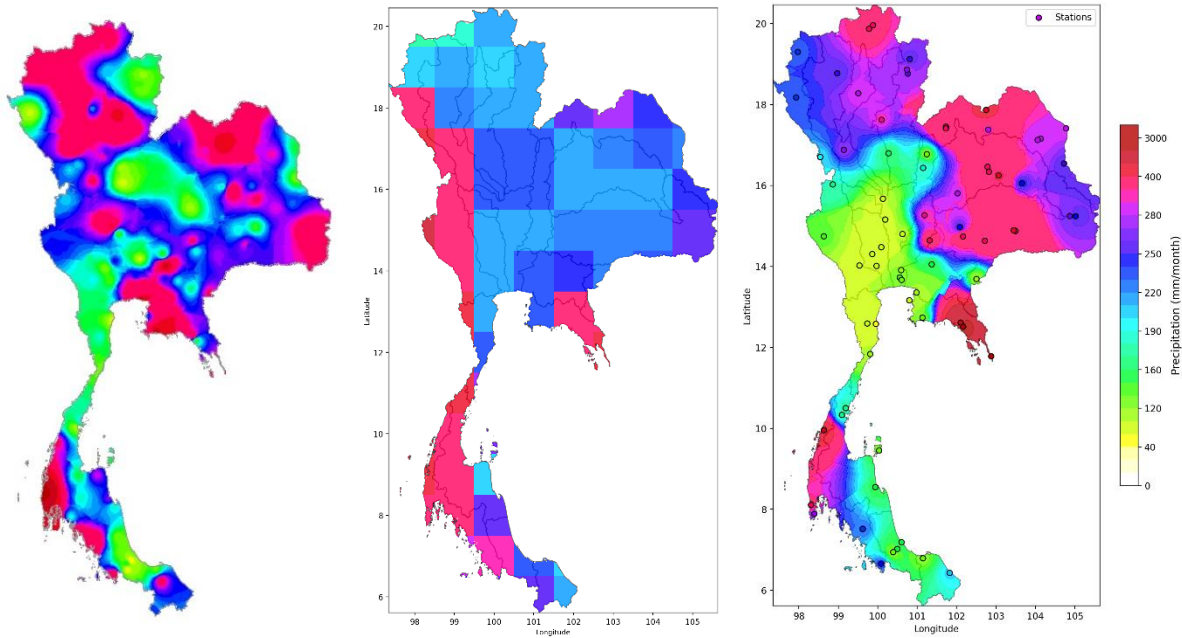


Figure 9. Monthly total precipitation for May 2025. Left: ground truth (average rainfall = 246.13 mm/month). Middle (prediction): SEAS5 (RMSE = 113.23 mm/month, average rainfall = 248.99 mm/month). Right (prediction): Attention-LSTM (Q = 95) (RMSE = 143.96 mm/month, average rainfall = 173.86 mm/month).

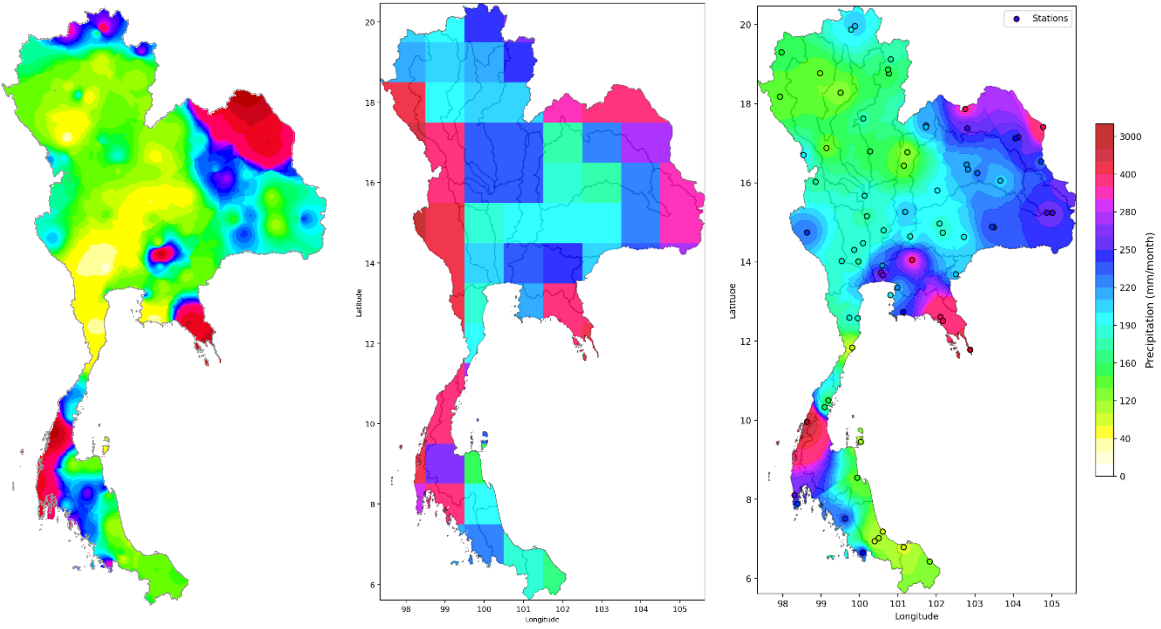


Figure 10. Monthly total precipitation for June 2025. Left: ground truth (average rainfall = 196.07 mm/month). Middle (prediction): SEAS5 (RMSE = 150.43 mm/month, average rainfall = 243.14 mm/month) Right (prediction): Attention-LSTM (Q = 95) (RMSE = 90.27 mm/month, average rainfall = 193.68 mm/month).

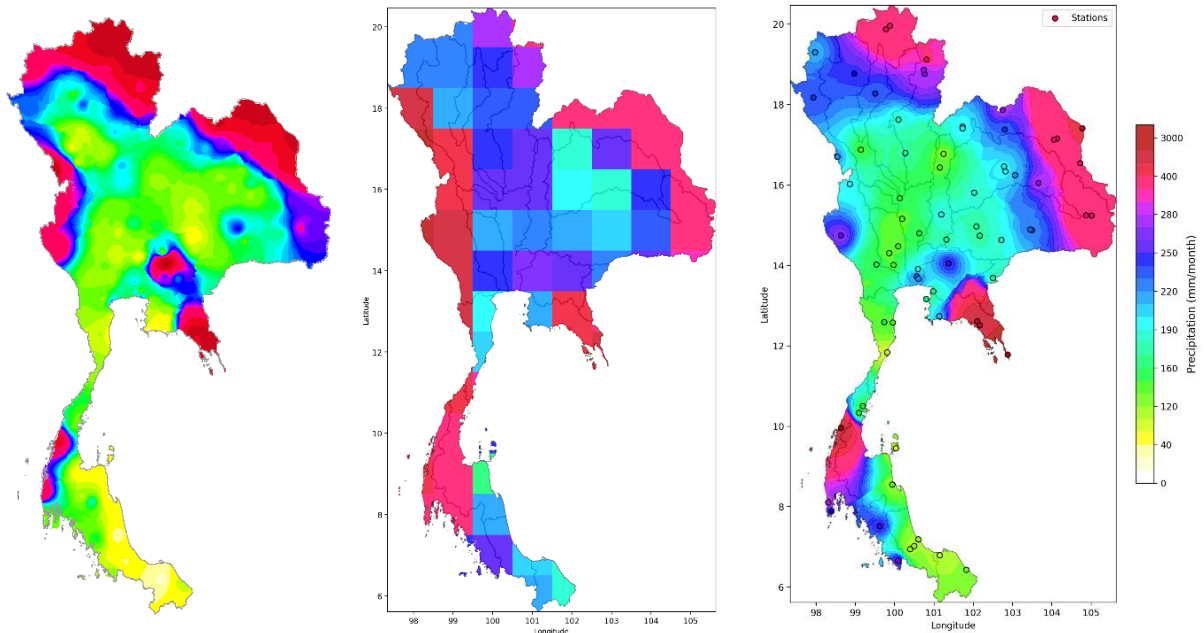


Figure 11. Monthly total precipitation for July 2025. Left: ground truth (average rainfall = 221.39 mm/month). Middle (prediction): SEAS5 (RMSE = 153.30 mm/month, average rainfall = 272.23 mm/month). Right (prediction): Attention-LSTM (Q = 95) (RMSE = 115.95 mm/month, average rainfall = 206.11 mm/month).

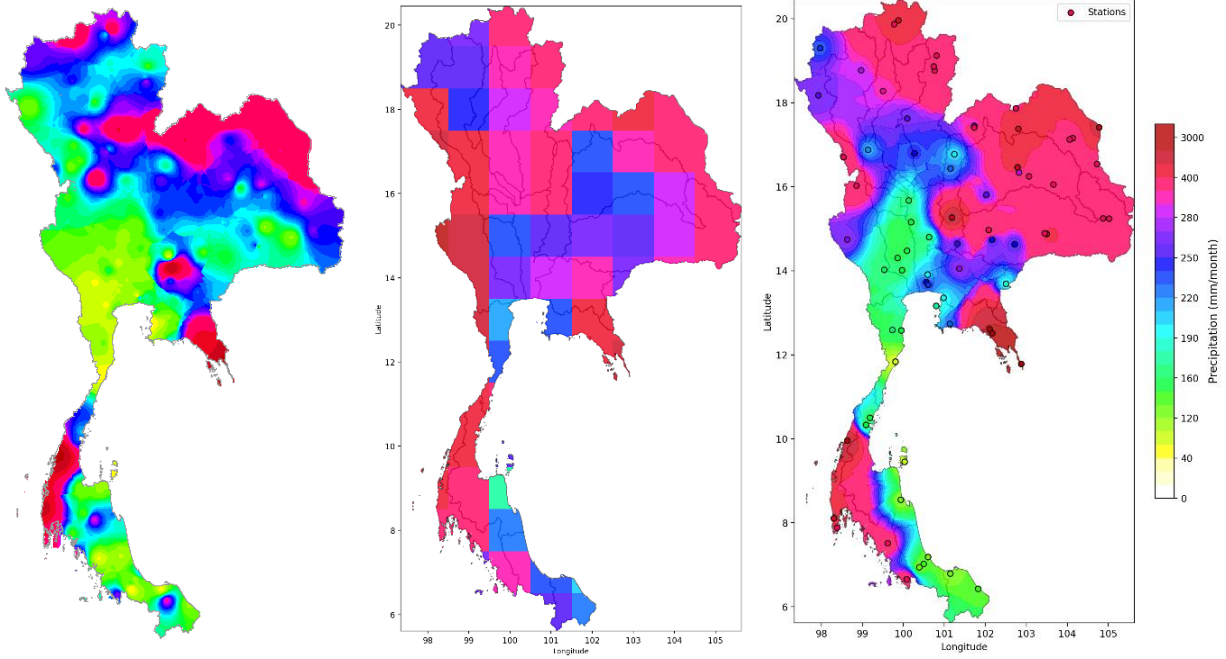


Figure 12. Monthly total precipitation for August 2025. Left: ground truth (average rainfall = 230.93 mm/month). Middle (prediction): SEAS5 (RMSE = 172.44 mm/month, average rainfall = 304.16 mm/month). Right (prediction): Attention-LSTM (Q = 95) (RMSE = 101.93 mm/month, average rainfall = 234.23 mm/month).

7 Conclusion and Future work

This work presents an interpretable graph-based model for long-range rainfall forecasting at gauge stations across Thailand, along with the forecasting system for real-world application. The proposed Attention-LSTM is constructed using statistical feature selection and hierarchical clustering to define static teleconnection graphs. The training process learns dynamic spatial and temporal weights given physics-informed edge features, enabling the model to discover nonlinear spatiotemporal dependencies using attention and LSTM. The model can produce forecasts 1–12 months ahead given historical rainfall and climate indices. To address extreme rainfall in the ML-model’s predictions, we propose a novel Peak-Over-Threshold, Spatial Season-aware GPD mapping that corrects predicted extremes falling into the distribution tails. This work emphasizes the importance of Earth system science in the relationships between meteorological climates and rainfall within explainable models and the correct implementation of ML methods rather than using them as black boxes.

Empirically, Attention-LSTM outperforms established baselines across most clusters and provides higher accuracy for extreme events in Clusters 1–4 on average. Performance gains are amplified across all clusters when pairing Attention-LSTM with orographic precipitation physics and Spatial Season-aware GPD mapping. These gains are particularly strong in southern of Thailand where extremes are frequent. In a few clusters, a simple LSTM remains competitive for RMSE or NSE, underscoring that post-processing and model choice should be tailored to local rainfall distributions rather than presuming models of graph attention or graph convolution

networks. In a real-world comparison against ECMWF SEAS5 seasonal forecasts, Attention-LSTM achieves lower average RMSE than SEAS5, with marginal performance drops during the transition from the monsoon onset to peak in April and May.

Several enhancements remain for future work. First, modeling temporal correlations could be improved to generate continuous forecast time series rather than discrete horizon steps. Second, replacing static graphs with learned or dynamic graphs could help capture evolving teleconnections. Third, augmenting spatial interpolation with ML-based methods such as DeepKriging should be explored for high-resolution maps in real-world applications. Finally, combining the Spatial Season-aware GPD mapping with probabilistic calibration could further improve extreme-value performance, supporting water-resource planning, reservoir operations, and climate-risk management.

Acknowledgements

The authors would like to express their gratitude to the Program Management Unit for Human Resources & Institutional Development, Research and Innovation (PMU-B), Ministry of Higher Education, Science, Research and Innovation, Thailand for funding this research.

References

Abatan, A. A., Collins, M., Babel, M. S., Khadka, D., & De Silva, Y. K. (2023). Sub-seasonal to seasonal drivers of dry extreme rainfall events over Northeast Thailand. *Frontiers in Climate*, 4, 1031226. <https://doi.org/10.3389/fclim.2022.1031226>

Allen, A., Markou, S., Tebbutt, W., et al. (2025). End-to-end data-driven weather prediction. *Nature*, 641, 1172–1179. <https://doi.org/10.1038/s41586-025-08897-0>

Amnuaylojaroen, T. (2021). Projection of precipitation extremes in Thailand under climate change scenario RCP8.5. *Frontiers in Environmental Science*, 9, 657810. <https://doi.org/10.3389/fenvs.2021.657810>

Bi, K., Xie, L., Zhang, H., Chen, X., Gu, X., & Tian, Q. (2022). Pangu-Weather: A 3D high-resolution model for fast and accurate global weather forecast. *arXiv*. <https://arxiv.org/abs/2211.02556>

Bonev, B., Kurth, T., Mahesh, A., Bisson, M., Kossaifi, J., Kashinath, K., Anandkumar, A., Collins, W. D., Pritchard, M. S., & Keller, A. (2025). FourCastNet 3: A geometric approach to probabilistic machine-learning weather forecasting at scale. *arXiv*. <https://arxiv.org/abs/2507.12144>

Camps-Valls, G., Fernández-Torres, M. Á., Cohrs, K. H., et al. (2025). Artificial intelligence for modeling and understanding extreme weather and climate events. *Nature Communications*, 16, 1919.

Camps-Valls, G., Gerhardus, A., Ninad, U., Varando, G., Martius, G., Balaguer-Ballester, E., Vinuesa, R., Diaz, E., Zanna, L., & Runge, J. (2023). Discovering causal relations and equations from data. *Physics Reports*, 1044, 1–68. <https://doi.org/10.1016/j.physrep.2023.10.005>

Chang, C.-H., Johnson, N. C., & Yoo, C. (2021). Evaluation of subseasonal impacts of the MJO/BSISO in the East Asian extended summer. *Climate Dynamics*, 56, 3553–3568. <https://doi.org/10.1007/s00382-021-05656-5>

Chen, J., Wang, X., & Xu, X. (2022). GC-LSTM: Graph convolution embedded LSTM for dynamic network link prediction. *Applied Intelligence*, 52(7), 7513–7528. <https://doi.org/10.1007/s10489-021-02518-9>

Cho, K., van Merriënboer, B., Gulcehre, C., Bahdanau, D., Bougares, F., Schwenk, H., & Bengio, Y. (2014). Learning phrase representations using RNN encoder–decoder for statistical machine translation. In A. Moschitti, B. Pang, & W. Daelemans (Eds.), *Proceedings of the 2014 Conference on Empirical Methods in Natural Language*

Processing (EMNLP) (pp. 1724–1734). Association for Computational Linguistics. <https://doi.org/10.3115/v1/D14-1179>

Chokngamwong, R., & Chiu, L. (2006). TRMM and Thailand daily gauge rainfall comparison. In Preprints of the 20th Conference on Hydrology. American Meteorological Society, Atlanta, GA.

Dechpichai, P., Jinapang, N., Yamphli, P., Polamnuay, S., Injan, S., & Humphries, U. (2022). Multivariable panel data cluster analysis of meteorological stations in Thailand for ENSO phenomenon. Mathematical and Computational Applications, 27(3). <https://doi.org/10.3390/mca27030037>

Du, D., Subramanian, A. C., Han, W., Ninad, U., & Runge, J. (2024). Causal analysis discovers an enhanced impact of tropical western Pacific on Indian summer monsoon subseasonal anomalies. Geophysical Research Letters, 51, e2023GL106431. <https://doi.org/10.1029/2023GL106431>

Fan, J., Li, Q., & Wang, Y. (2017). Estimation of high-dimensional mean regression in the absence of symmetry and light-tail assumptions. Journal of the Royal Statistical Society: Series B, 79, 247–265.

Fuentes-Franco, R., Giorgi, F., Coppola, E. *et al.* The role of ENSO and PDO in variability of winter precipitation over North America from twenty first century CMIP5 projections. *Clim Dyn* 46, 3259–3277 (2016). <https://doi.org/10.1007/s00382-015-2767-y>

Granger, C. W. J. (1969). Investigating causal relations by econometric models and cross-spectral methods. *Econometrica*, 37(3), 424–438.

Hammond, D. K., Vanderghenst, P., & Gribonval, R. (2011). Wavelets on graphs via spectral graph theory. *Applied and Computational Harmonic Analysis*, 30(2), 129–150. <https://doi.org/10.1016/j.acha.2010.04.005>

Hochreiter, S., & Schmidhuber, J. (1997). Long short-term memory. *Neural Computation*, 9(8), 1735–1780. <https://doi.org/10.1162/neco.1997.9.8.1735>

Huang, B., Liu, C., Banzon, V., Freeman, E., Graham, G., Hankins, B., Smith, T., & Zhang, H. (2021). Improvements of the Daily Optimum Interpolation Sea Surface Temperature (DOISST) version 2.1. *Journal of Climate*, 34(8), 2923–2939. <https://doi.org/10.1175/JCLI-D-20-0166.1>

Huber, P. J. (1964). Robust estimation of a location parameter. *The Annals of Mathematical Statistics*, 35, 73–101. <https://doi.org/10.1214/aoms/1177703732>

Johnson, S. J., Stockdale, T. N., Ferranti, L., Balmaseda, M. A., Molteni, F., Magnusson, L., Tietsche, S., Decremer, D., Weisheimer, A., Balsamo, G., Keeley, S. P. E., Mogensen, K., Zuo, H., & Monge-Sanz, B. M. (2019). SEAS5: The new ECMWF seasonal forecast system. *Geoscientific Model Development*, 12(3), 1087–1117. <https://doi.org/10.5194/gmd-12-1087-2019>

Khedari, J., Sangprajak, A., & Hirunlabh, J. (2002). Thailand climatic zones. *Renewable Energy*, 25(2), 267–280.

KIKUCHI, Kazuyoshi (2021). The Boreal Summer Intraseasonal Oscillation (BSISO): A Review. 99(4). <https://doi.org/10.2151/jmsj.2021-045>

Kitson, N., Constantinou, A., Guo, Z., Liu, Y., & Chobtham, K. (2023). A survey of Bayesian network structure learning. *Artificial Intelligence Review*, 56(8), 8721–8814. <https://doi.org/10.1007/s10462-022-10351-w>

Kipf, T. N., & Welling, M. (2017). Semi-supervised classification with graph convolutional networks. In 5th International Conference on Learning Representations (ICLR 2017), Conference Track Proceedings. OpenReview. <https://openreview.net/forum?id=SJU4ayYg1>

Kurth, T., Subramanian, S., Harrington, P., Pathak, J., Mardani, M., Hall, D., Miele, A., Kashinath, K., & Anandkumar, A. (2023). FourCastNet: Accelerating global high-resolution weather forecasting using adaptive

Fourier neural operators. In Proceedings of the Platform for Advanced Scientific Computing Conference (PASC '23) (Article 13, pp. 1–11). Association for Computing Machinery. <https://doi.org/10.1145/3592979.3593412>

Lam, R., Sanchez-Gonzalez, A., Willson, M., Wirnsberger, P., Fortunato, M., Alet, F., Ravuri, S., Ewalds, T., Eaton-Rosen, Z., Hu, W., Merose, A., Hoyer, S., Holland, G., Vinyals, O., Stott, J., Pritzel, A., Mohamed, S., & Battaglia, P. (2023). Learning skillful medium-range global weather forecasting.

Lucarini, Valerio & Faranda, Davide & Freitas, Ana & Freitas, Jorge & Kuna, Tobias & Holland, Mark & Nicol, Matthew & Todd, Mike & Vaienti, Sandro. (2016). Extremes and Recurrence in Dynamical Systems. 10.1002/9781118632321.index.

Maraun, D. (2016). Bias correcting climate change simulations: A critical review. *Current Climate Change Reports*, 2, 211–220. <https://doi.org/10.1007/s40641-016-0050-x>

Moten, S., Yunus, F., Ariffin, M., Burham, N., Diong, J. Y., Adam, M., & Yip, S. (2014). Statistics of northeast monsoon onset, withdrawal and cold surges in Malaysia (Technical report).

Pareja, A., Domeniconi, G., Chen, J., Ma, T., Suzumura, T., Kanezashi, H., Kaler, T., Schardl, T., & Leiserson, C. (2020). EvolveGCN: Evolving graph convolutional networks for dynamic graphs. *Proceedings of the AAAI Conference on Artificial Intelligence*, 34(4), 5363–5370. <https://doi.org/10.1609/aaai.v34i04.5943>

Ravuri, S., Lenc, K., Willson, M., et al. (2021). Skilful precipitation nowcasting using deep generative models of radar. *Nature*, 597, 672–677.

Runge, J., Bathiany, S., Boltt, E., et al. (2019). Inferring causation from time series in Earth system sciences. *Nature Communications*, 10, 2553.

Saha, A., & Ravela, S. (2024). Statistical-physical adversarial learning from data and models for downscaling rainfall extremes. *Journal of Advances in Modeling Earth Systems*, 16, e2023MS003860. <https://doi.org/10.1029/2023MS003860>

Scarselli, F., Tsoi, A. C., & Hagenbuchner, M. (2018). The Vapnik–Chervonenkis dimension of graph and recursive neural networks. *Neural Networks*, 108, 248–259. <https://doi.org/10.1016/j.neunet.2018.08.010>

Shan, R., Ning, H., Xu, Q., Su, X., Guo, M., & Jia, X. (2025). Physics-informed and explainable graph neural networks for generalizable urban building energy modeling. *Applied Sciences*, 15(16), 8854. <https://doi.org/10.3390/app15168854>

Smith, R. B. (2003). A linear upslope-time-delay model for orographic precipitation. *Journal of Hydrology*, 282(1–4), 2–9. [https://doi.org/10.1016/S0022-1694\(03\)00248-8](https://doi.org/10.1016/S0022-1694(03)00248-8)

Sun, Q., et al. (2021). A global, continental, and regional analysis of changes in extreme precipitation. *Journal of Climate*, 34(1), 243–258.

Ting, Y.-S. (2024). Why machine learning models systematically underestimate extreme values. *arXiv*. <https://doi.org/10.48550/arXiv.2412.05806>

Veličković, P., Cucurull, G., Casanova, A., Romero, A., Liò, P., & Bengio, Y. (2018). Graph attention networks. *arXiv*. <https://arxiv.org/abs/1710.08415>

Verma, Y., Heinonen, M., & Garg, V. (2024). ClimODE: Climate and weather forecasting with physics-informed neural ODEs. In *Proceedings of the International Conference on Learning Representations (ICLR 2024)*.

Waqas, M., Humphries, U. W., & Hlaing, P. T. (2024). Time series trend analysis and forecasting of climate variability using deep learning in Thailand. *Results in Engineering*, 24, 102997.

Waqas, M., Li, P. T. H., Humphries, U. W., & co-authors. (2024). Advancements in daily precipitation forecasting: A deep dive into daily precipitation forecasting hybrid methods in the tropical climate of Thailand. *MethodsX*, 12, 102757. <https://doi.org/10.1016/j.mex.2024.102757>

Waqas, M., Wannasingha Humphries, U., Chueasa, B., & Wangwongchai, A. (2025). Artificial intelligence and numerical weather prediction models: A technical survey. *Natural Hazards Research*, 5(2), 306–320. <https://doi.org/10.1016/j.nhres.2024.11.004>

Waqas, M., Humphries, U. W., Hlaing, P. T., et al. (2023). Potential of artificial intelligence-based techniques for rainfall forecasting in Thailand: A comprehensive review. *Water*, 15(16), 2979. <https://doi.org/10.3390/w15162979>

Wu, T., Chen, F., & Wan, Y. (2018). Graph attention LSTM network: A new model for traffic flow forecasting. In 2018 5th International Conference on Information Science and Control Engineering (ICISCE) (pp. 241–245). IEEE. <https://doi.org/10.1109/ICISCE.2018.00059>

Zheng, C., Fan, X., Wang, C., & Qi, J. (2019). GMAN: A graph multi-attention network for traffic prediction. *arXiv*. <https://arxiv.org/abs/1911.08415>

Appendix A.

Table A1. The maximum and minimum of average Pearson correlations (R) of climate index and rainfall across stations for each cluster between 2014-2024 used in experiments.

Cluster	Climate Index	Max of R	Min of R
1	DMI	0.64	-0.54
	MEIV2	0.59	-0.46
	NE	0.54	0.54
	ONI	0.68	-0.73
	PDO	0.62	-0.48
	RMM1	-0.40	-0.40
	SWM	-0.41	-0.60
2	DMI	0.64	-0.55
	ONI	0.68	-0.75
	PDO	0.72	-0.58
3	DMI	0.62	-0.68
	MEIV2	0.73	-0.57
	NE	0.52	0.52
	ONI	0.70	-0.62
	PDO	0.55	-0.69
	RMM1	-0.48	-0.48
	SWM	-0.40	-0.65
4	BSISO1	0.73	0.42
	DMI	0.70	-0.81
	MEIV2	0.58	-0.59
	NE	0.67	-0.45
	ONI	0.55	-0.66
	PDO	0.57	-0.53
	RMM1	-0.42	-0.71
	SWM	-0.67	-0.83
5	BSISO1	0.80	0.43
	MEIV2	0.61	-0.79
	NE	0.60	-0.53
	ONI	0.65	-0.53
	RMM1	-0.42	-0.69
	SWM	-0.54	-0.80
6	BSISO1	0.64	0.44
	DMI	0.54	-0.66
	NE	0.49	-0.49
	ONI	0.45	-0.62
	RMM1	-0.40	-0.56
	SWM	-0.52	-0.73
7	BSISO1	0.66	0.40
	DMI	0.51	-0.67
	NE	0.42	-0.43
	RMM1	-0.47	-0.52
	SWM	-0.47	-0.74
8	BSISO1	0.64	0.47
	DMI	0.59	-0.67
	MEIV2	0.47	-0.46
	NE	0.41	-0.45
	ONI	0.42	-0.49
	RMM1	-0.43	-0.65

	SWM	-0.43	-0.77
9	BSISO1	0.65	0.48
	DMI	0.62	-0.65
	MEIV2	0.50	-0.49
	ONI	0.50	-0.51
	RMM1	-0.47	-0.62
	SWM	-0.58	-0.75
10	BSISO1	0.61	0.50
	DMI	0.72	-0.75
	MEIV2	0.47	-0.80
	NE	0.74	-0.41
	ONI	0.55	-0.64
	PDO	0.57	0.44
	RMM1	0.48	-0.66
	SWM	-0.48	-0.81
12	BSISO1	0.64	0.43
	DMI	0.49	-0.64
	NE	0.45	-0.44
	ONI	0.53	-0.52
	RMM1	-0.49	-0.59
	SWM	-0.49	-0.68

Table A2. The average p-values given Granger causality test of climate index (Y) for each cluster between 2014-2024 used in experiments.

Cluster	Climate Index	Lag (month)	P-value
1	DMI	1	0.082
1	PDO	1	0.056
1	MEIV2	2	0.095
2	MEIV2	2	0.052
3	PDO	1	0.073
3	MEIV2	2	0.090
8	MEIV2	3	0.059
9	MEIV2	3	0.077
10	PDO	1	0.064

Table A3. The GPD fitted parameters of given MLE for each station and its season in Clusters 1 and 8 where percentile Q is 95%.

Node	Season	Observation				Prediction of Attention-LSTM			
		u	ξ	a_u	exceedances	u	ξ	a_u	exceedances
Cluster 1									
551203	Dry	147.7	0.23	113.83	26	124.4	-0.30	23.65	23
	NE monsoon	538.5	-0.04	257.69	20	426.5	-0.30	35.22	18
	SW monsoon	183.4	0.17	48.68	33	246.8	-0.24	65.98	29
552201	Dry	220.7	0.63	111.16	26	170.2	-0.31	29.45	23
	NE monsoon	750.9	-0.17	281.13	20	589.3	-0.46	41.74	18
	SW monsoon	210.8	0.26	38.56	33	308.5	-0.39	60.54	29
564201	Dry	141.4	-0.29	111.27	26	230.9	-0.36	31.58	23

	NE monsoon	353.7	-0.10	114.43	20	184.4	-0.59	97.44	18
	SW monsoon	398.9	0.05	90.17	33	352.9	-0.06	26.45	29
564202	Dry	177.3	-0.03	89.38	26	264.4	-0.47	38.16	23
	NE monsoon	402.3	0.17	81.40	20	216.0	-0.47	87.73	18
	SW monsoon	498.9	-0.40	126.08	33	399.7	-0.09	31.27	29
567201	Dry	164.9	0.08	64.14	26	221.1	-0.29	25.29	23
	NE monsoon	345.8	-0.25	102.35	20	201.6	-0.23	59.84	18
	SW monsoon	362.7	-0.12	115.68	33	330.9	-0.05	29.83	29
570201	Dry	220.3	-0.13	78.44	26	231.2	-0.03	20.67	23
	NE monsoon	364.5	0.04	56.73	20	217.5	-0.07	63.71	18
	SW monsoon	378.3	-0.19	93.15	33	350.3	-0.12	27.38	29
Cluster 8									
352201	Dry	29.3	-0.15	34.08	26	41.28	-0.05	30.1	23
	Monsoon onset	241.1	-0.48	115.73	20	245.64	0.20	15.0	17
	Monsoon peak	404.3	-0.15	110.69	33	308.54	-0.56	53.1	29
353201	Dry	27.6	0.14	23.44	26	42.57	-0.12	18.4	23
	Monsoon onset	187.4	-1.03	214.52	20	183.01	-0.10	16.6	17
	Monsoon peak	262.0	-0.04	79.55	33	233.90	-0.39	37.6	29
353301	Dry	27.9	0.06	24.36	26	42.70	-0.22	22.4	23
	Monsoon onset	193.8	-0.76	142.99	20	177.74	0.05	13.9	17
	Monsoon peak	264.0	-0.10	69.41	33	227.43	-0.63	50.9	29
354201	Dry	30.1	0.12	15.34	26	35.36	-0.20	27.2	23
	Monsoon onset	190.2	-0.29	96.61	20	206.39	-0.15	19.0	17
	Monsoon peak	309.5	-0.09	107.08	33	260.41	-0.46	43.2	29
381201	Dry	27.2	-0.01	27.51	26	43.27	-0.15	19.6	23
	Monsoon onset	178.3	-0.50	87.72	20	181.18	0.13	11.3	17
	Monsoon peak	279.0	-0.10	79.64	33	230.69	-0.48	43.2	29
381301	Dry	28.7	0.03	29.07	26	38.73	-0.27	22.4	23
	Monsoon onset	187.8	-0.27	76.38	20	170.35	-0.20	20.7	17
	Monsoon peak	252.0	0.15	64.82	33	216.66	-1.11	80.3	29
387401	Dry	23.1	0.24	14.21	26	39.77	-0.21	24.5	23
	Monsoon onset	188.3	-0.13	80.22	20	188.02	-0.21	18.1	17
	Monsoon peak	283.8	-0.24	98.03	33	244.73	-0.36	38.5	29
403201	Dry	23.8	0.10	20.43	26	37.49	-0.28	23.2	23
	Monsoon onset	160.7	-0.53	72.47	20	164.98	-0.08	16.1	17
	Monsoon peak	270.3	-0.12	74.56	33	223.86	-0.62	39.0	29
426401	Dry	26.4	0.45	14.13	26	36.51	-0.18	21.4	23
	Monsoon onset	160.9	-0.34	64.57	20	166.11	0.21	8.4	17
	Monsoon peak	248.9	-0.05	93.26	33	218.20	-0.75	50.5	29
431201	Dry	28.6	-0.33	30.55	26	42.50	0.01	13.8	23
	Monsoon onset	186.2	-1.32	91.27	20	156.96	-0.05	14.3	17
	Monsoon peak	248.4	-0.08	65.46	33	213.17	-0.54	35.5	29
431301	Dry	45.3	-0.39	45.57	26	49.06	-0.18	17.3	23
	Monsoon onset	173.6	-0.36	77.30	20	155.59	-0.04	14.3	17
	Monsoon peak	244.5	-0.28	78.43	33	216.79	-0.86	37.8	29
431401	Dry	34.1	0.25	18.48	26	43.19	-0.17	15.7	23
	Monsoon onset	148.0	-0.21	66.08	20	150.80	-0.13	16.8	17
	Monsoon peak	229.2	-0.34	87.36	33	201.87	-0.76	49.5	29
432201	Dry	31.3	0.11	21.96	26	43.26	-0.09	22.4	23
	Monsoon onset	203.0	-0.06	42.47	20	202.45	-0.17	24.5	17
	Monsoon peak	318.2	0.11	72.20	33	260.41	-1.20	84.4	29
432301	Dry	26.1	-0.20	36.80	26	44.69	0.03	17.9	23
	Monsoon onset	195.0	-0.03	59.25	20	201.64	-0.11	23.1	17
	Monsoon peak	305.2	0.06	78.83	33	258.39	-0.79	62.1	29
436401	Dry	26.7	-0.32	53.21	26	47.98	-0.21	18.9	23
	Monsoon onset	182.7	-0.41	99.63	20	168.49	-0.38	24.9	17
	Monsoon peak	265.3	-0.52	88.58	33	231.73	-0.64	42.8	29

Appendix B.

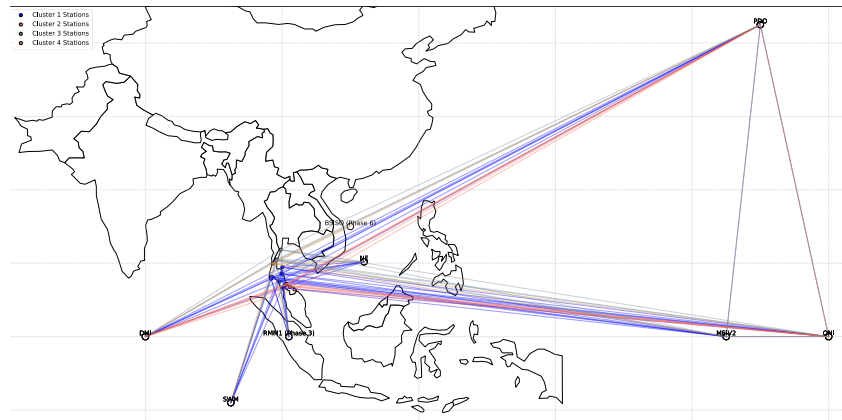


Figure B1. Examples of reanalysis graph-based structure of GNN models showed their stations as nodes and their teleconnections as edges in Clusters 1-4

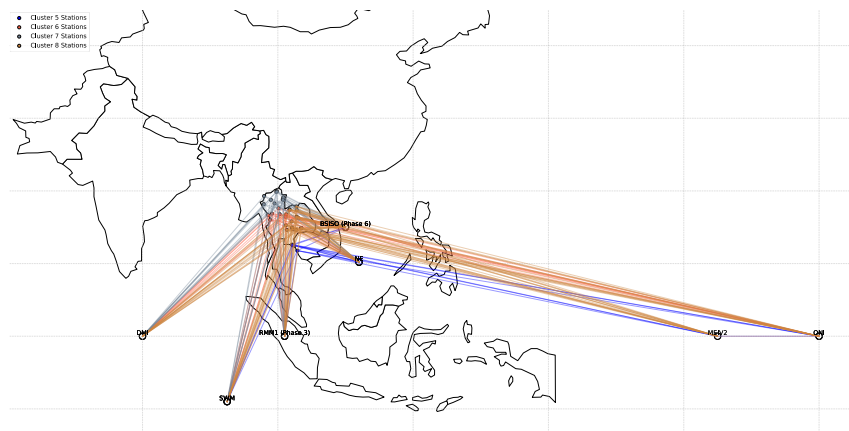


Figure B2. Examples of reanalysis graph-based structure of GNN models showed their stations as nodes and their teleconnections as edges in Clusters 5-8

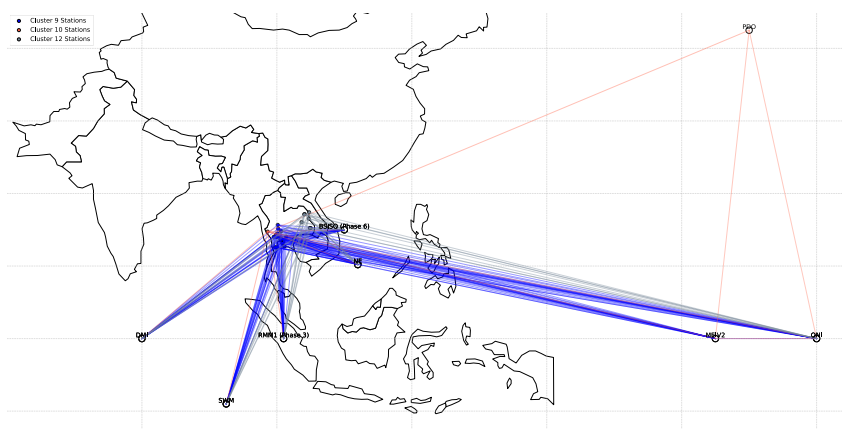


Figure B3. Examples of reanalysis graph-based structure of GNN models showed their stations as nodes and their teleconnections as edges in Clusters 9-12